AFRL-RX-WP-TP-2008-4352

MODELING AND SIMULATION OF TEXTURE EVOLUTION DURING THE THERMOMECHANICAL PROCESSING OF TITANIUM ALLOYS (PREPRINT)

S.L. Semiatin, S.V. Shevchenko, O.M. Ivasishin, M.G. Glavicic, Y.B. Chun, and S.K. Hwang

Metals Branch
Metals, Ceramics, and NDE Division

SEPTEMBER 2008

Approved for public release; distribution unlimited.

See additional restrictions described on inside pages

STINFO COPY

AIR FORCE RESEARCH LABORATORY
MATERIALS AND MANUFACTURING DIRECTORATE
WRIGHT-PATTERSON AIR FORCE BASE, OH 45433-7750
AIR FORCE MATERIEL COMMAND
UNITED STATES AIR FORCE

REPORT DOCUMENTATION PAGE

Form Approved
OMB No. 0704-0188

The public reporting burden for this collection of information is estimated to average 1 hour per response, including the time for reviewing instructions, searching existing data sources, searching existing data sources, gathering and maintaining the data needed, and completing and reviewing the collection of information. Send comments regarding this burden estimate or any other aspect of this collection of information, including suggestions for reducing this burden, to Department of Defense, Washington Headquarters Services, Directorate for Information Operations and Reports (0704-0188), 1215 Jefferson Davis Highway, Suite 1204, Arlington, VA 22202-4302. Respondents should be aware that notwithstanding any other provision of law, no person shall be subject to any penalty for failing to comply with a collection of information if it does not display a currently valid OMB control number. **PLEASE DO NOT RETURN YOUR FORM TO THE ABOVE ADDRESS**.

1. REPORT DATE *(DD-MM-YY)*
September 2008

2. REPORT TYPE
Technical Paper Preprint

3. DATES COVERED *(From - To)*

4. TITLE AND SUBTITLE
MICROSTRUCTURE EVOLUTION DURING WARM WORKING OF Ti-6Al-4V WITH A COLONY ALPHA MICROSTRUCTURE (PREPRINT)

5a. CONTRACT NUMBER
In-house

5b. GRANT NUMBER

5c. PROGRAM ELEMENT NUMBER
62102F

6. AUTHOR(S)
S.L. Semiatin (AFRL/RXLMP)
S.V. Shevchenko and O.M. Ivasishin (Institute for Metal Physics)
M.G. Glavicic (Rolls-Royce Corporation)
Y.B. Chun and S.K. Hwang (Inha University)

5d. PROJECT NUMBER
4347

5e. TASK NUMBER
RG

5f. WORK UNIT NUMBER
M02R2000

7. PERFORMING ORGANIZATION NAME(S) AND ADDRESS(ES)

Metals Branch (AFRL/RXLMP)
Metals, Ceramics, and NDE Division
Materials and Manufacturing Directorate
Wright-Patterson Air Force Base, OH 45433-7750
Air Force Materiel Command, United States Air Force

Institute for Metal Physics

Rolls-Royce Corporation

Inha University

8. PERFORMING ORGANIZATION REPORT NUMBER
AFRL-RX-WP-TP-2008-4352

9. SPONSORING/MONITORING AGENCY NAME(S) AND ADDRESS(ES)
Air Force Research Laboratory
Materials and Manufacturing Directorate
Wright-Patterson Air Force Base, OH 45433-7750
Air Force Materiel Command
United States Air Force

10. SPONSORING/MONITORING AGENCY ACRONYM(S)
AFRL/RXLMP

11. SPONSORING/MONITORING AGENCY REPORT NUMBER(S)
AFRL-RX-WP-TP-2008-4352

12. DISTRIBUTION/AVAILABILITY STATEMENT
Approved for public release; distribution unlimited.

13. SUPPLEMENTARY NOTES
Paper submitted to the ASM Handbook, Vol. 22–Modeling and Simulation: Processing of Metallic Materials. PAO Case Number: WPAFB 08-5083; Clearance Date: 18 Aug 2008. The U.S. Government is joint author of this work and has the right to use, modify, reproduce, release, perform, display, or disclose the work. Paper contains color.

14. ABSTRACT
The development of crystallographic texture, the preferred orientation of grains in a polycrystalline aggregate, during thermomechanical processing (TMP) can play an important role with regard to the secondary-forming response (e.g., deep drawing of sheet) and service performance (e.g., strength, elastic modulus, ductility, fracture toughness) of metallic materials. Crystallographic texture, or simply texture for succinctness, may arise as a result of large-strain deformation, dynamic/static recrystallization, grain growth, or phase transformation [1]. A second form of anisotropy, mechanical texturing or mechanical fibering, refers to the alignment of microstructure, inclusions, etc., during deformation processes and may also affect mechanical properties such as ductility and fracture toughness. This latter form of texture is not discussed in the present article.

15. SUBJECT TERMS
crystallographic texture, mechanical texturing, mechanical fibering, titanium alloy, thermomechanical processing

16. SECURITY CLASSIFICATION OF:

a. REPORT	b. ABSTRACT	c. THIS PAGE
Unclassified	Unclassified	Unclassified

17. LIMITATION OF ABSTRACT:
SAR

18. NUMBER OF PAGES
80

19a. NAME OF RESPONSIBLE PERSON (Monitor)
Sheldon L. Semiatin

19b. TELEPHONE NUMBER *(Include Area Code)*
N/A

Standard Form 298 (Rev. 8-98)
Prescribed by ANSI Std. Z39-18

Modeling and Simulation of Texture Evolution during the Thermomechanical Processing of Titanium Alloys

S.L. Semiatin, S.V. Shevchenko*, O.M. Ivasishin*, M.G. Glavicic**
Y.B. Chun***, and S.K. Hwang***

Air Force Research Laboratory, AFRL/RXLM,
Wright-Patterson Air Force Base, OH 45433-7817
* G.V. Kurdyumov Institute for Metal Physics, Kyiv, Ukraine 03142
** Rolls-Royce Corporation, P.O. Box 420, Indianapolis, IN 46206-0420
*** Division of Materials Science and Engineering,
Inha University, Incheon, Korea 402-751

INTRODUCTION

The development of *crystallographic texture*, the preferred orientation of grains in a polycrystalline aggregate, during thermomechanical processing (TMP) can play an important role with regard to the secondary-forming response (e.g., deep drawing of sheet) and service performance (e.g., strength, elastic modulus, ductility, fracture toughness) of metallic materials. Crystallographic texture, or simply texture for succinctness, may arise as a result of large-strain deformation, dynamic/static recrystallization, grain growth, or phase transformation [1]. A second form of anisotropy, *mechanical texturing* or *mechanical fibering*, refers to the alignment of microstructure, inclusions, etc., during deformation processes and may also affect mechanical properties such as ductility and fracture toughness. This latter form of texture is not discussed in the present article.

Because of its technological importance, a number of modeling and simulation techniques have been formulated to describe the evolution of crystallographic texture [2, 3]. A majority of these techniques have been developed for predicting textures in face-centered-cubic (fcc) and body-centered-cubic (bcc) metals. Considerably less work has been done in the area of hexagonal-close-packed (hcp) materials, let alone two-phase alloys one of whose phases is hcp, such as is the case for a number of industrially-important titanium alloys.

Unalloyed titanium and titanium alloys comprise a class of material for which texture can be unusually strong and therefore is very important with regard to mechanical properties [4, 5]. The tendency to form strong textures results principally from the low symmetry of the hcp crystal structure which characterizes many titanium alloys at low-temperatures, the limited number of slip and twinning systems that can be activated to accommodate imposed deformation of hcp crystals, and the allotropic transformation of titanium from the bcc beta phase (at high temperatures) to the hcp alpha phase (at low temperatures). The first two of these factors play an important role with regard to the formation of deformation texture in both alpha and alpha/beta titanium alloys. The nature of prior deformation and the allotropic transformation affect transformation-texture development in both alpha/beta and near-beta titanium alloys.

In the broad sense, crystallographic texture is but one, albeit an important one, of the many attributes that are needed to fully characterize the metallurgical state of a material. Thus, the modeling and simulation of texture evolution for titanium alloys is often tightly coupled to microstructure evolution. This article focuses on a number of problems for titanium alloys in which such coupling is critical in the development of quantitative models. For some phenomena, such as spheroidization, coarsening, etc, it is not as important to model microstructure and texture evolution simultaneously. Such situations are summarized in the article "Modeling of Microstructure Evolution during the Thermomechanical Processing of Titanium Alloys" in this volume.

A number of general considerations related to the characterization, modeling, and simulation of texture are treated in other articles in this volume; e.g., “Crystallographic Texture,” “Crystal-Plasticity Fundamentals”, “Self-Consistent Texture Modeling,” and “Crystal-Plasticity FEM”. Hence, this article focuses solely on aspects pertaining to titanium and titanium alloys. To this end, the key aspects of phase equilibria, the description of crystallographic orientations, and slip/twinning behavior of importance for titanium alloys are summarized first. Subsequent sections of this article describe the modeling and simulation of recrystallization and grain growth of single-phase beta and single-phase alpha titanium and deformation- and transformation-texture evolution in two-phase (alpha/beta) titanium alloys.

FUNDAMENTAL CONSIDERATIONS FOR TITANIUM

The description of phase equilibria, crystallography, and deformation behavior of titanium and titanium alloys is of great importance with regard to understanding and modeling texture evolution. Each of these topics is briefly discussed in this section.

Phase Equilibria/Phase Transformations

Microstructure *and* texture evolution and control in titanium alloys is heavily dependent on the allotropic transformation from the hcp crystal structure (denoted as alpha phase) found at low temperatures to a bcc crystal structure (denoted as beta phase) at high temperatures [6]. For pure titanium, this occurs at 882°C. In many titanium alloys, the beta phase is partially stabilized at lower temperatures, and the equilibrium volume fractions of alpha and beta vary with temperature. The temperature at which a specific alloy becomes entirely beta (i.e., alpha + beta → beta) is called the beta transus. The conditions used for hot working and heating/heat treatment are often selected relative to the beta-transus temperature.

There are a number of important classes of titanium alloys, whose designations reflect the relative volume fraction of beta retained at room temperature. These include beta and near-beta alloys and near-alpha and alpha/beta alloys [7, 8]. Beta and near-beta alloys have moderate to large amounts of beta-stabilizing elements such as vanadium, molybdenum, tungsten, niobium, chromium, and iron. The beta transi of near-beta alloys are typically in the range of 700 to 850°C [7]. Near-alpha and alpha/beta alloys have large amounts of alpha-stabilizing elements such as aluminum; the beta transi of near-alpha and alpha/beta alloys are usually of the order of 950 to 1050°C [8].

The cooling of alpha/beta alloys from a temperature above the beta transus or the aging of beta-annealed-and-water-quenched near-beta alloys results in the decomposition of metastable beta. The alpha that is formed has a lath or platelet morphology. The orientation of the alpha is related to that of the parent beta by a classical Burgers relation [9]. The single close-packed plane in the hcp alpha phase (i.e., the basal plane) is parallel to one of the six close-packed planes in the bcc beta phase. In addition, one of the three close-packed ("**a**") directions in the basal plane of the alpha is parallel to one of the two close-packed directions lying within the specific close-packed plane in the beta (Figure 1). Thus, decomposition of a beta grain may give rise to one or more of 12 (= 6 x 2) possible alpha-phase variants, each with its own orientation within the beta grain. It is rare that a specific beta grain would contain a large number of the 12 possible alpha variants. Often, a subset of these may be found due to a variant-selection process. Various factors may affect variant selection. These include stress (which may be applied macroscopically or develop as a result of temperature gradients, for example) [10] and, if the beta has been hot worked, residual dislocation substructure on the activated slip systems. Possible variant-selection rules are discussed in the section below on the modeling of transformation texture in alpha/beta titanium alloys.

Crystallography and Description of Orientation

Descriptions of crystallography and the orientations of bcc beta and hcp alpha are critical to the modeling and simulation of texture evolution in titanium alloys.

Crystallography is rather simple for the bcc phase whose unit cell comprises atoms at each corner and an atom at the center of a cube (Figure 1b). Using standard miller indices for cubic crystals, the three principal directions are parallel to the cube edges, i.e., [100], [010], and [001]. Similarly, the planes comprising cube faces are denoted (100), (010), and (001). Each of the six close-packed planes contains 4 corner atoms and the central atom and are denoted as {110} - type planes, e.g., (110) and $(\bar{1}10)$. The four close-packed directions are the cube diagonals and are of the type <111>, e.g., the $[1\bar{1}1]$ and $[\bar{1}11]$ directions lying in the (110) plane.

The crystallography of the hcp unit cell shows less symmetry than the bcc unit cell (Figure 1a). The *four* miller indices for hcp crystals denote relative lengths/inverse intercepts along the three close-packed directions and the normal to the close-packed plane. The close-packed (basal) plane is thus (0001) and its normal is [0001], known also as the c axis. The three close-packed directions lying in the basal plane are denoted a_1, a_2, and a_3, or $[2\bar{1}\bar{1}0]$, $[\bar{1}2\bar{1}0]$, $[\bar{1}\bar{1}20]$, respectively. Because these three directions lie in the same plane at 120° angles to each other, the third index of the miller indices for hcp crystals is always equal to minus the sum of the first two indices. Other planes of importance comprise the prism planes ($\{10\bar{1}0\}$ type) and various pyramidal planes, the most important of which are the $\{10\bar{1}1\}$ planes, which contain the directions consisting of the vector sum **c** + **a**, i.e., the $<11\bar{2}3>$ directions.

The description of texture relies on quantifying the orientation of bcc and hcp crystal axes relative to an orthogonal set of material (sample) reference directions, e.g., X, Y, Z (or RD, TD, SN for sheet/plate materials). For the bcc phase, the crystal axes are taken to be the [100], [010], and [001] directions. Several different choices are used for the orthogonal set for hcp crystals. The most common consists of the $[2\bar{1}\bar{1}0]$, $[01\bar{1}0]$, and [0001] directions.

The 3 x 3 rotation (orientation) matrix *g*, consisting of the cosines of the angles between the crystal axes and the material reference directions, is used to quantify the orientation of a crystal relative to the material reference directions. The *ij* th member of this matrix is the cosine of the angle between the *i* th crystal axis and the *j* th sample reference direction (Figure 2a) [1, 11]:

$$g = \begin{pmatrix} \cos\alpha_1 & \cos\beta_1 & \cos\gamma_1 \\ \cos\alpha_2 & \cos\beta_2 & \cos\gamma_2 \\ \cos\alpha_3 & \cos\beta_3 & \cos\gamma_3 \end{pmatrix} = \begin{pmatrix} g_{11} & g_{12} & g_{13} \\ g_{21} & g_{22} & g_{23} \\ g_{31} & g_{32} & g_{33} \end{pmatrix}. \qquad (1)$$

The description of orientation via the 9-parameter rotation matrix is actually an over-specification inasmuch as the sample reference directions can be brought into coincidence with the crystal axes (or vice versa) by *three* independent rotations. The three rotation angles are known as Euler angles. Although a number of conventions have been used to specify Euler angles, the most common is that due to Bunge [1, 11, 12]. The three Bunge Euler angles are denoted φ_1, Φ, and φ_2, and comprise the following successive rotations (Figure 2b):

- Rotation of φ_1 about Z/SN, transforming the Y/TD direction into Y'/TD' and the X/RD direction into X'/RD'.
- Rotation of Φ about X'/RD', transforming the Y'/TD' direction into Y''/TD'' and the Z/SN direction into the Z''/SN''.
- Rotation of φ_2 about Z''/ND''.

The elements of the rotation matrix (Equation (1)) are related to the Euler angles by the following set of relations [11]:

$$\begin{aligned}
g_{11} &= \cos\varphi_1 \cos\varphi_2 - \sin\varphi_1 \sin\varphi_2 \cos\Phi \\
g_{12} &= \sin\varphi_1 \cos\varphi_2 + \cos\varphi_1 \sin\varphi_2 \cos\Phi \\
g_{13} &= \sin\varphi_2 \sin\Phi \\
g_{21} &= -\cos\varphi_1 \sin\varphi_2 - \sin\varphi_1 \cos\varphi_2 \cos\Phi \\
g_{22} &= -\sin\varphi_1 \sin\varphi_2 + \cos\varphi_1 \cos\varphi_2 \cos\Phi \\
g_{23} &= \cos\varphi_2 \sin\Phi \\
g_{31} &= \sin\varphi_1 \sin\Phi \\
g_{32} &= -\cos\varphi_1 \sin\Phi \\
g_{33} &= \cos\Phi
\end{aligned} \tag{2}$$

The orientation relation between the reference axes and an arbitrarily-oriented crystal *or* the misorientation between two adjacent crystals can also be represented as a single rotation about a specific axis. For the case of the misorientation between two adjacent crystals 1 and 2, for example, a misorientation matrix Q_{12} is calculated first:

$$Q_{12} = g_1^T g_2, \tag{3}$$

in which g_1^T denotes the transpose of the rotation matrix for grain 1, and g_2 is the rotation matrix for grain 2. The misorientation angle θ is then given by the following expression [11]:

$$\cos \theta = (g_{11} + g_{22} + g_{33} - 1)/2 \tag{4}$$

The components *r* of the axis of rotation (relative to the axes of one of the crystals) are the following [11]:

$$\begin{aligned} r_1 &= g_{23} - g_{32} \\ r_2 &= g_{31} - g_{13} \\ r_3 &= g_{12} - g_{21} \end{aligned} \tag{5}$$

In Equations (4) and (5), the quantities g_{ij} are the elements of the misorientation matrix Q_{12}.

The overall texture of *polycrystalline* aggregates is represented by pole figures or orientation distribution functions (ODFs). A pole figure is a 2D stereographic projection of the probability of finding a specified crystallographic direction (”pole”) at various orientations relative to the sample reference directions. Typical pole figures for beta titanium are 100, 110, and 111. For alpha titanium, 0001, $10\bar{1}0$, $11\bar{2}0$, and $10\bar{1}1$ pole figures are used to quantify texture. Similarly, an ODF summarizes the probability of finding crystals with given Euler angles relative to the sample reference directions.

Slip/Twinning Systems

Alpha Phase. Deformation textures in unalloyed titanium and two-phase titanium alloys tend to be strong because of the low symmetry of hcp crystals and the limited number of modes of deformation due to crystallographic slip or twinning.

The most common slip systems for hcp titanium consist of basal <a> (slip on the basal plane along an <a> direction), prism <a> (slip on a prism plane along an <a> direction), and pyramidal <c+a> (slip on pyramidal planes along a <c+a> direction) (Figure 3). In the case of an arbitrary imposed deformation, five independent slip systems must be activated within each grain of a polycrystalline aggregate. Because there are only two independent basal <a> systems and two independent prism <a> systems, pyramidal <c+a> slip must also be activated. Compressive or tensile deformation along the c axis of an hcp crystal is enabled by <c+a> slip.

Deformation of hcp titanium by <c+a> slip involves stresses usually much higher than those required for basal <a> or prism <a> slip. Hence, twinning may provide alternate, softer modes to accommodate deformation along the c axis, particularly under ambient or cold-working temperatures. The key twinning systems (denoting the twinning plane by the first index and the twinning direction by the second) include $\{11\bar{2}2\} < \bar{1}\bar{1}23 >$, which provides a compressive strain along the c axis, and $\{10\bar{1}2\} < \bar{1}011 >$ and $\{11\bar{2}1\} < \bar{1}\bar{1}26 >$, each of which gives a tensile strain along the c axis [13, 14].

The analysis of deformation texture often involves the application of the strain (or stress) tensor transformation law from a set of reference axes to the hcp crystal axes. To determine the appropriate direction cosines (Equation (1)) it is often simplest to apply the dot product formula. In this case, the use of an *orthogonal* set of reference axes for hexagonal crystals is preferable. As mentioned above, a typical choice of axes comprises the $[2\bar{1}\bar{1}0]$, $[01\bar{1}0]$, and [0001] directions; i.e., $[2\bar{1}\bar{1}0]$ is represented as [100], $[01\bar{1}0]$ as [010], and [0001] as [001]. With this choice, the miller indices for various slip systems in an equivalent orthogonal system can be calculated (Table I).

Beta Phase. Bcc metals such as beta titanium are known to deform by slip along <111> slip directions. However, the slip plane(s) are not well defined. Some have modeled deformation texture evolution for bcc metals such as beta titanium assuming pencil glide, i.e., slip on any plane containing a <111> direction [16, 17]. Others have assumed a slightly more restrictive approach, assuming slip only on {110}, {112}, and {123} planes [18, 19]. In yet other work, it has been suggested that the active slip planes, particularly at intermediate temperatures, are of the {112} type [20].

TEXTURE EVOLUTION DURING RECRYSTALLIZATION AND GRAIN GROWTH

Modeling of recrystallization and grain growth of single-phase-beta or single-phase-alpha titanium has a number of important industrial applications. These include the recrystallization and grain growth of alpha/beta and beta titanium alloys during heat treatment in the single-phase beta field (i.e., above the beta-transus temperature) and the recrystallization and grain growth of alpha titanium during heat treatment in the alpha phase field. Grain growth of alloys with no prior hot work during beta annealing is perhaps the simplest problem in texture evolution for titanium alloys and is discussed first. Subsequently, the simulation of coupled recrystallization and grain growth of materials that have been prior hot- or cold-worked is addressed.

Beta Grain Growth

Beta annealing is often used for alpha/beta titanium alloys to develop a transformed-beta microstructure for fracture-critical aerospace applications. Beta annealing is also applied as a solution treatment for beta and near-beta alloys prior to aging in the alpha/beta phase field. In both cases, the control of the beta grain size can be very important.

A number of measurements of beta-grain-growth kinetics for alloys such as Ti-6Al-4V and Ti-5Mo-5V-5Al-1Fe-1Cr (VT22) have shown substantial deviations from the parabolic behavior which characterizes classical *normal* grain growth (i.e., $d^n \sim t$, in which d denotes the grain size, t is time, and n is the grain-growth exponent) [21-25]. Specifically, periods of rapid and slow growth have been observed during both isothermal heat treatments and processes involving continuous heating (Figure 4). Furthermore, grain-growth kinetics have been found to vary quite noticeably in different lots of a given alloy such as Ti-6Al-4V with identical composition and initial microstructure, but different with initial textures. These observations can therefore be ascribed to initial texture and the evolution of texture during grain growth. Such texture-controlled grain growth is a result of the anisotropy in energy and mobility of beta grain boundaries.

Texture-controlled grain growth during beta annealing of titanium alloys has been simulated using both the Monte-Carlo (Potts) and phase-field-modeling approaches. In the work of Ivasishin, *et al.* [24, 25], for example, the Monte-Carlo (MC) method was utilized; a detailed description of the MC technique is contained in the article “Monte-Carlo Models for Grain Growth and Recrystallization” in this volume. Suffice it to say, the MC formulation of Ivasishin, *et al.* was similar to that in prior efforts with regard to (1) the calculation of energy before and after an elementary orientation "flip" (except that the trial orientation was taken to be that of a randomly-chosen neighboring site and not the entire model lattice) and (2) the quantitative description of the probability for atoms at/near the grain boundaries to change their orientations. However, a number of improvements were incorporated to obtain quantitative information on the coupling of grain growth and texture evolution. These improvements included (1) the application of a 3D, rather than a 2D, analysis, (1) the use of a large number of possible orientations defined by their respective Euler angles, (3) the ability to input measured or hypothetical textures using pole figures or orientation-distribution functions (ODFs), and (4) extensive post-processor software enhancements to quantify intermediate and final grain-size and grain-boundary-misorientation distributions, textures/volume fractions of texture components, etc. To simplify the calculations for large 3D modeling domains, the separate effects of grain-boundary energy and mobility were combined into a single effective mobility parameter.

To obtain insight into the specific interaction of texture and grain growth, Ivasishin, *et al.* [24, 25] applied the 3D code to a number of special cases, including grain growth in (1) an initially textured or untextured material with a misorientation-dependent or independent grain-boundary mobility and (2) a material with an initial two-component texture and misorientaion-dependent grain-boundary mobility. Sample MC results for the material with two initial texture components (denoted A and B) are shown in Figures 5-7. The MC-simulated kinetics revealed periods of fast and slow grain growth (Figure 5a), similar to experimental observations. As seen in (100) pole figures

(Figure 5b), there were also pronounced variations in texture as grain growth occurred. (Only the (100) poles (and not the (010) and (001) poles) are shown for the sake of clarity.) The texture changes were characterized by periodic interchanges of the volume fractions of the two components. A comparison of Figures 5a and 5b indicates that the periods of rapid grain growth were associated with the times (~15 MCS and ~1200 MCS).at which the volume fractions of the two texture components were approximately equal and there was thus a large fraction of high-angle boundaries

The MC-simulated texture evolution for the two-component case can be explained as follows. Because of their lower volume fraction, the A grains initially had a much higher probability of being surrounded by B grains rather than by other A grains and thus of having high mobility A-B boundaries. Hence, small A grains were rapidly consumed by large B grains, but large A grains were able to grow rapidly. Because the B grains were in contact preferentially with other B grains, they had mainly low mobility B-B boundaries; therefore, most of the B grains participated only slightly in the initial stages of grain growth. This led to a very different grain-size distribution for the modeling domain as a whole (Figure 6a) compared to that for those grains with the A texture component (Figure 6b). After the A grains had consumed a majority of the volume, the growth rate of the A grains decreased, because there was now a high probability that each was surrounded by other A grains. As B had become the minority component, the growth rate of B grains exceeded that of the A grains. Over long times, such phenomena produced cyclic changes in the relative volume fractions of the A and B texture components.

MC predictions of the periodic evolution of a two-component texture [25] mirror *deterministic* numerical calculations, such as those of Lücke and his coworkers [26, 27] (Figure 7). These earlier calculations were based on the classical expression for the velocity v of a grain boundary between grains ν and μ, i.e.,

$$v_{\nu\mu} = 2M_{\nu\mu}\gamma_{\nu\mu}\left(R_{\nu}^{-1} - R_{\mu}^{-1}\right), \tag{6}$$

in which $M_{\nu\mu}$, $\gamma_{\nu\mu}$, R_{ν}, and R_{μ} denote the grain-boundary mobility, grain-boundary surface energy, and radii of the adjacent grains. For the case of a two-component texture [26], the calculations comprise (1) the discretization of the grain-size distributions for each of the two texture components into bins and (2) applying a relation of the form of Equation (6) for the grains in each bin of each texture component. The value of $M\gamma$ used in these expressions is an average of those for AA and AB interfaces (for A grains) or for BB and AB interfaces (for B grains) weighted by the volume fractions of A and B grains.

A comparison of MC predictions of texture-controlled grain growth to experimental observations has shown only qualitative agreement [24] to date. The differences can be attributed largely to the dearth of quantitative data on grain-boundary energy and mobility as a function of misorientation for titanium alloys. Furthermore, it has been shown using 3D MC simulations that periods of rapid and slow grain growth may also be due to the anisotropy of boundary properties associated with tilt-twist character/boundary inclination [28-30].

In similar work, Ma and his coworkers [31, 32] simulated texture-controlled grain growth during beta annealing of Ti-6Al-4V using the phase-field method. The effect of grain-boundary energy/mobility and specific type of initial texture on grain-growth kinetics and the evolution of the different texture components were evaluated.

Recrystallization of Beta Titanium

The recrystallization of beta titanium plays a key role in breaking down coarse ingot structures to obtain semi-finished billet products of essentially all conventional titanium alloys as well as in refining the beta grain size during the TMP of plate and sheet product of beta and near-beta titanium alloys. Modeling efforts in this area have begun only recently and have focused primarily on static recrystallization of beta titanium alloys.

Obtaining a uniform (statically) recrystallized microstructure in beta-rich titanium alloys can be very difficult. The challenge arises from the non-uniformity in stored energy within grains (from prior hot deformation in the beta phase field) as well as from grain to grain. Static recrystallization kinetics are thus different in different areas, giving rise to simultaneous propagation of the recrystallization front in some areas and grain growth in other, previously recrystallized, areas. Two approaches have been proposed to address problems of this sort. One involves the development of phenomenological processing maps that delineate combinations of forging and heat treatment parameters that produce uniform recrystallization [33]. A second approach, which is just emerging, comprises the application of modeling techniques such as the Monte-Carlo (MC) and cellular-automata (CA) techniques [34-36]. The CA method [35, 36] has been applied to treat dynamic recrystallization. The specific method involves tracking the generation/storage and annihilation of dislocations, nucleation events, and migration of a recrystallization front. The details of the relationship between the orientations of the deformed matrix and nuclei and the mobility of different types of boundaries have yet to be incorporated, however, thus limiting the application of CA techniques for quantitative texture predictions. These drawbacks have been remedied using the MC technique, at least for static recrystallization problems, and thus attention below is focused on this method.

Formulation of Monte-Carlo Simulations. An MC routine [34] has been formulated and applied to provide insight into static recrystallization and grain growth in beta titanium alloys. The calculation procedure in already *recrystallized* regions is similar to that for standard MC simulations of grain growth in that the probability P for re-orientation during an elementary flip trial at site *i* is taken to be the following:

$$P = U(\theta)\, W(\theta) \exp(-\Delta E_L / k_b T_s) \qquad \text{for } \Delta E_L > 0 \qquad (7a)$$

and

$$P = U(\theta)\, W(\theta) \qquad \text{for } \Delta E_L \leq 0\,, \qquad (7b)$$

In Equations (7a) and (7b), U and W denote the relative (normalized) grain-boundary mobility (M/M_{max}) and energy (γ/γ_{max}) as a function of the scalar misorientation θ between the initial and trial orientations; ΔE_L is the change in system energy before and after the flip trial; and k_b is Boltzmann's constant. In the absence of stored energy due to cold or hot working, the system energy E_L is the total grain-boundary energy and is typically given by the following relation for 3D MC simulations:

$$E_L = \frac{1}{2} \sum_{i=1}^{N} \left(\sum_{j=1}^{26} W(\theta)[1 - \delta(q_i, q_j)] \right) \qquad (7c)$$

Here, the first summation is taken over the total number N of lattice sites in the simulation; the second summation is taken over the 26 first, second, and third nearest neighbors (for a simple cubic lattice) whose orientations/states are taken to be those specifically possible for the trial flip; q_i and q_j denote the orientations of sites *i* and *j*; and $\delta(q_i, q_j)$ denotes the kronecker delta (= 1 for $q_i = q_j$ and = 0 for $q_i \neq q_j$). In Equation (7a), T_s represents the simulation temperature (not the real workpiece temperature); k_bT_s is an energy that defines the thermal fluctuations/"noise" present in MC simulations. When the probability P (Equations (7a) and (7b)) is greater than that obtained from a random-number generator that produces values between 0 and 1, the flip is retained; i.e., boundary migration occurs. Otherwise, the original orientation/state is restored.

The boundary energy in Equation (7) is often assumed to follow the classic Read-Shockley behavior for low-angle boundaries ($\theta < 15°$) and exhibit a constant (maximum) energy for non-special, high-angle boundaries ($\theta \geq 15°$) (Figure 8a):

$$\gamma = \gamma_{max}\left(\frac{\theta}{\theta_{max}}\right)\left[1 - \ln\left(\frac{\theta}{\theta_{max}}\right)\right] \qquad \text{for } \theta < 15^\circ \qquad (8a)$$

$$\gamma = \gamma_{max} \qquad \text{for } \theta \geq 15^\circ \qquad (8b)$$

The mobility dependence on misorientation ($M(\theta)$) can be based on specific measurements or the formulation of Rollett and Holm [37] (Figure 8a):

$$M(\theta) = M_{max}\left\{1 - m_a \exp\left[\left(-\frac{\theta}{10^\circ}\right)^3\right]\right\} \qquad (9)$$

In this expression, M_{max} is the maximum mobility (corresponding to non-special, high-angle boundaries), and the parameter m_a is set equal to 0 or 1 for the isotropic and the most anisotropic case, respectively.

For flip trials focusing on a site *i* located *at the recrystallization front*, Equation (7a) is replaced by an expression of the following form:

$$P = U(\theta)\ \frac{H_i}{H_{max}}\ \exp(-\Delta E_L/k_bT)\ . \qquad (10)$$

Here, H_i denotes the stored energy at site *i*, and H_{max} is the maximum stored energy in the material; the grain-boundary energy in the pre-multiplier term is neglected because its value is usually several orders of magnitude less than the typical levels of stored work associated with dislocations. An expression similar to Equation (7c), but which incorporates the stored energy H_i/H_{max}, is used to estimate E_L and hence ΔE_L associated with the flip trial; i.e., recrystallization and migration of the recrystallization front. Various spatial dependences of stored energy can be used. These include uniform stored energy within each grain (with each grain's energy scaled by its Taylor Factor, M_T) and a stored-work distribution whose magnitude decreases from a maximum at the grain boundary toward the center of the grain (Figure 8b).

In the MC simulations described in Reference 34, nucleation was assumed to occur at a constant rate (10^{-4} nuclei/ MU^3 per MCS; MU ≡ model lattice unit/ lattice spacing) at grain boundaries and local regions of high stored energy. *Oriented nucleation* was introduced by assigning various probabilities for the possible misorientations between the deformed matrix and the recrystallization nucleus. Specifically, it was assumed that nuclei were either randomly-oriented or formed a $\Sigma9$, $\Sigma19$, or $\Sigma27$ boundary with the deformed matrix grain, thus giving rise to misorientation angles/rotation axes of 39°<110>, 26.5°<110>, or 35°<110>, respectively. These orientations are typical for the recrystallization of bcc metals [38, 39].

Monte-Carlo Simulation Predictions. A number of interesting predictions were obtained by Ivasishin, *et al.* [34] from 3D MC simulations using the above formulation.

The simulation materials / initial textures comprised the cold-drawn, beta titanium alloy Timetal LCB (Ti-4.5Fe-6.8Mo-1.5Al) with partial fibers denoted as β and η [1] and hot-rolled sheet of VT22 (Ti-5Al-5Mo-5V-1Cr-1Fe) with an α fiber [1]. Some of the key findings were as follows:

- Oriented nucleation assuming a preponderance of $\Sigma 9$ nuclei gives rise to a noticeably different texture (relative to the deformation texture) after recrystallization is complete, not surprisingly.
- The nature of the stored energy distribution can have a strong effect on recrystallization kinetics. This behavior can be demonstrated using three cases each assuming randomly-oriented nuclei and the same initial *total* stored energy, but with one of three different initial stored-energy distributions: (A) uniform within each grain, scaled by M_T, (B) energy gradient varying smoothly within each grain with a minimum of 0.7 H_{max}, and (C) energy gradient within each grain and with a number of local maxima (Figure 8b). The most rapid recrystallization rate is found for the third instance due to the large number of recrystallization nuclei (Figure 9). The recrystallization rate for the second case is initially high due to the high level of stored energy near the grain boundaries, but decreases substantially at long times; this behavior is accentuated in Avrami plots of the recrystallization kinetics (Figure 9b).
- The mobility of special boundaries can have a pronounced effect on microstructure/texture evolution and recrystallization kinetics. These dependences can be illustrated using two simulations both of which assume oriented nucleation with nuclei probabilities P of $P(\Sigma 9) = 0.4$, $P(\Sigma 19) = 0.3$, $P(\Sigma 27) = 0.3$, and

P (random) = 0; in one case, the special boundaries have the same mobility and in the other the mobility is 40 pct. higher than that of non-special, high-angle boundaries. A noticeable difference in microstructure and recrystallized fraction after a time of 100 MCS is evident in simulation predictions for the two cases (Figure 10).

- Oriented nucleation has a strong effect on recrysttallization texture which in turn affects subsequent grain-growth kinetics, as discussed earlier in the section on the modeling of beta grain growth.

Recrystallization of Alpha Titanium

Significant progress has been made in modeling the recrystallization of alpha titanium. The principal focus in this area has been on the *static* recrystallization of cold- or warm-worked *unalloyed* (alpha) titanium.

Experimental Observations. Modeling and simulation of the static recrystallization of alpha titanium has been guided by detailed characterization of the deformed microstructure and experimental observations of recrystallization kinetics, etc. For both commercial-purity (CP) and high-purity unalloyed titanium, very inhomogeneous microstructures are developed as a result of the competition between crystallographic slip and twinning at cold-, and to a lesser extent warm-, working temperatures [13, 14, 40, 41]. At cold-working temperatures, for example, twinning is activated at very low strains (~0.05) and reaches a saturation level at effective strains of ~0.3-0.6 in both uniaxial compression and rolling due to a Hall-Petch type of strengthening. Furthermore, as shown by Salem, *et al.* [13] for a highly-textured lot of pure titanium, the amount of twinning that is activated is heavily dependent on the imposed strain state. Imposed strains that require compressive or tensile strains along the c-axis of many of the grains in a polycrystalline aggregate lead to high volume fractions of twins. Those strain states that require limited extension or compression along the c axis result in the accommodation of the imposed deformation primarily by slip processes in the majority of the grains.

Chun, *et al* [14, 40] have done extensive characterization of the microstructure developed during the cold-rolling and recrystallization annealing of CP titanium (CP Ti) sheet. It was found that cold rolling to a moderate reduction ($\leq$ 40 pct.) activates slip and mechanical twinning, primarily $\{11\bar{2}2\} < \bar{1}\bar{1}23 >$ compressive twins and $\{10\bar{1}2\} < \bar{1}011 >$ tensile twins (Figure 11a). The formation of twins results in an inhomogeneous microstructure, in which regions containing twins are refined and the grains which deform primarily by slip remain relatively coarse (Figure 11b). The occurrence of twinning can weaken the starting texture leading to a moderate basal texture (Figure 12). Above 40 pct. reduction, during which deformation by slip predominates, a split-basal texture typical of cold-rolled hcp metals (with a principal ODF component of φ_1=0°, Φ=35-90°, φ_2=30°) is developed.

During subsequent recrystallization annealing of CP Ti at temperatures of the order of 600°C, twinned grains, which contain high stored energy and numerous high-angle boundaries, become the preferential sites for nucleation. Despite their impingement, the recrystallized grains grow quickly, consuming the neighboring deformed regions in short times (~15 minutes). The coarse, elongated remnant grains with low stored energy hinder the recrystallization process and require considerably longer times (of the order of 100 minutes) to be consumed. Although the overall recrystallization kinetics may exhibit a sigmoidal behavior, the corresponding Avrami plot is bi-linear (Figure 13a, b).

During recrystallization, the cold-rolling texture diminishes in intensity, and a recrystallization-texture component (φ_1=15°, Φ=35°, φ_2=35°) appears. The recrystallization texture component strengthens during the subsequent grain growth stage. This behavior can be attributed to the growth of larger-than-average grains of this particular crystallographic orientation.

Formulation for Monte-Carlo Simulations. Similar to the work of Ivasishin, *et al.* [34] dealing with the recrystallization of beta titanium, Chun, *et al.* [42] developed and applied a 2D MC code to describe the recrystallization of cold-worked alpha titanium. The key components of this formulation consist of descriptions of (1) the stored energy associated with the deformed (cold-worked) state, (2) the decrease in stored energy during annealing due to static recovery, (3) nucleation behavior, and (4) the flip probability for recrystallization/migration of the recrystallization front.

The spatial distribution of cold-work can be quantified by deformation models such as crystal-plasticity techniques [39, 43] or direct measurements based on image-quality maps derived from electron-backscatter-diffraction (EBSD) [44, 45]. Because of the complexity of the microstructure developed during the cold deformation of CP Ti, the EBSD image-quality-map approach is preferable. The technique utilizes EBSD Kikuchi-pattern bands whose sharpness is dependent on elastic strains which distort the crystal lattice. Chun, *et al.* used the following relation to quantify this effect:

$$H_i = k\left(1 - \frac{IQ_i}{f \cdot IQ_{max}}\right) , \tag{11}$$

in which H_i and IQ_i denote the stored energy (in arbitrary units) and the image quality, respectively, at MC lattice site *i*; IQ_{max} is the maximum value of the image quality; and k and f are constants that specify the upper and lower bounds for the stored-energy distribution. In line with other measurements, Chun, *et al.* chose k = 70 and f = 1.3, respectively, which resulted in stored-energy values ranging from 16 to 65. An example image-quality map for CP Ti rolled to a thickness reduction of 60 pct. is shown in Figure 11c. Regions with fine microstructure (developed in grains that underwent both twinning and slip) have high stored energy. The coarse remnants of the initial grain structure (which deformed only by slip) exhibit low values of stored energy.

Static recovery is described using the following relation:

$$H_{new} = (1\text{-}b)H_{old} , \tag{12}$$

in which H_{old} and H_{new} are the stored energy before and after recovery. This relation quantifies the exponential decay of stored energy with time, which is typical of the static recovery of metals [46].

In the work of Chun, *et al.* [42], nucleation was assumed to comprise site saturation; i.e., all nuclei were assumed to be formed at the beginning of the annealing process. The nucleation sites were placed either randomly in the lattice or at sites with high-stored energy. For the latter, high-stored-energy-nucleation (HSEN), case, 1000 lattice sites among those belonging to the upper 1 pct. of stored energy were chosen. The stored energies of these nuclei were set to zero, and their orientations were taken to be the same as that for the lattice site in the deformed state.

The probability for recrystallization/migration of the recrystallization front can be treated in a manner analogous to that embodied in Equation (10). In the work of Chun, *et al.* [42], however, an explicit expression for strain-induced migration of the recrystallization front between sites *i* and *j* as a function of the local variation in stored energy and the grain-boundary mobility was utilized, i.e.:

$$v_{ij} = a_r \cdot \Delta H_{ij} \cdot M. \qquad (13)$$

In this equation, v_{ij} denotes a velocity that varies between 0 and 1; a_r is a constant that ensures a realistic rate of recrystallization corresponding to the range of energy differences ΔH_{ij} between sites *i* and *j* (e.g., 0 to 65), and M is the mobility (as a function of misorientation) as given in Equation (9). When v_{ij} is greater than the probability obtained from a random-number generator that produces values between 0 and 1, the recrystallized grain grows at the expense of the deformed site *j*. As a consequence, the stored energy of site *j* is reset to zero, and the orientation of site *j* is changed to that of site *i*.

The calculation procedure in already *recrystallized* regions is similar to that for standard MC simulations of grain growth.

Monte-Carlo Simulation Predictions. The MC simulations of Chun, *et al.* [42] illustrate the effects of concurrent recovery, the spatial distribution of nuclei, the heterogeneous distribution of stored energy, and anisotropy of grain-boundary energy and mobility on static recrystallization kinetics and texture evolution, and thus aid in the interpretation of observations for CP Ti. For the ideal case of no recovery, site saturation with randomly-placed nuclei, uniformly distributed stored energy, and isotropic boundary properties, MC predictions reveal a linear Avrami plot with a slope *p* of ~2.15 (Figure 13c), in good agreement with the classical Johnson-Mehl-Avrami-Kolmogorov (JMAK) prediction of 2.0.

A number of useful predictions can be obtained for special cases in which only one parameter (i.e., recovery, nuclei distribution, stored-energy distribution) is varied relative to the special case that mirrors JMAK behavior. When static recovery is included in MC simulations, for example, Avrami curves show a *negative* deviation from the linear JMAK behavior. The deviation becomes more dramatic as the parameter b (Equation (12)) is increased, accentuating the rate of recovery and thus the loss of the driving force for boundary migration associated with the stored energy. The distribution of the nuclei can also lead to deviations from the linear JMAK trend. When the nuclei are uniformly or heterogeneously distributed rather than at random locations, positive or negative deviations, respectively, are predicted. The range of stored energy (e.g., $15<H<65$, $20<H<86$, $50<H<92$) has little influence on recrystallization kinetics. Increasing the average level of stored energy reduces the recrystallization time, but the distribution per se does not result in deviations from linear JMAK behavior. When these various factors and anisotropic grain-boundary properties are all incorporated into the MC simulation, Avrami plots which mirror experimental observations are obtained (e.g., Figures 13b versus Figure 13c).

The spatial and temporal information from MC simulations provides a useful tool for investigating the source of deviations from linear JMAK behavior. Such interpretations often involve “microstructural-path” analysis; e.g., determination of the average velocity V_{CH} of the recrystallization front as a function of the recrystallized fraction X, using the the Cahn-Hagel relation [47]:

$$v_{CH} = \frac{1}{S_v} \cdot \frac{dX}{dt} \,, \tag{14}$$

Here, S_v and t denote the total area of the recrystallization front per unit volume and the time, respectively. For 2D MC simulations, S_v and t can be replaced by the total *length* of the recrystallization front per unit area, L_A, and the simulation time in Monte-Carlo steps (MCS), respectively.

As examples, plots of V_{CH}, L_A, and the recrystallization rate ($\Delta X/\Delta MCS$) as a function of X are shown in Figure 14. For the ideal case giving rise to linear JMAK kinetics (Figure 14a), the recrystallization front moves at a nearly constant speed during the entire recrystallization process; the parameters L_A and $\Delta X/\Delta MCS$ exhibit maxima at $X \sim 0.42$. By contrast, for the simulation involving recovery, heterogeneous nucleation at non-uniformly distributed sites of high stored energy, and anisotropic grain-boundary properties (Figure 14b), the front velocity increases rapidly during the very early stage of recrystallization, and then decreases; L_A and $\Delta X/\Delta MCS$ both reach maxima at lower values of the recrystallized fraction (i.e., $X \sim 0.3$) than the classic JMAK case. This situation corresponds to the Avrami plot in Figure 13c. Thus, a negative deviation in recrystallization kinetics can be correlated to the onset of decreasing L_A at a lower value of X compared to that for JMAK kinetics or an average velocity of the recrystallization front which decreases with time.

MC simulations also provide an invaluable tool to investigate the coupling of microstructure and texture evolution during recrystallization of a material such as CP Ti whose as-deformed condition is so complex. For instance, observed and simulated microstructures for recrystallization of CP titanium cold rolled to a thickness reduction of

60 pct. and annealed at 600°C show excellent agreement (Figure 15). These results illustrate the heterogeneity of recrystallization at short times in local regions with high stored energy and the subsequent grain growth in these areas during longer times at which the balance of the microstructure with lower initial stored energy is still undergoing recrystallization. Similar remarks apply to predictions of texture, quantified for example by orientation-distribution functions (ODFs) (Figure 16). For CP Ti, the *as-deformed* texture used for MC simulations (Figure 16b, top) was obtained by EBSD over a limited area of observation (120 μm × 100 μm) and thus differs slightly from that obtained by x-ray diffraction (Fig. 16a, top); i.e., the peak intensity of the XRD analysis appeared at φ_1=0°, Φ=35° and φ_2=30°, while that of the EBSD analysis was at φ_1=0°, Φ=55° and φ_2=30°. However, the experimental and MC-predicted recrystallization textures (Figures 16a, bottom and 16b, bottom, respectively) both show a weakening of the φ_1=0°, Φ=50~90° and φ_2=30° orientations and a strengthening of φ_1=0~30°, Φ=20~40° and φ_2=30° orientations. The strengthened texture component corresponds to the orientation of regions of high stored energy in the as-cold rolled CP Ti. This finding tends to support the MC-simulation assumption of identical orientations for both the deformed material and the nuclei and the importance of nucleation behavior in controlling the recrystallization textures of alpha titanium.

SIMULATION OF DEFORMATION TEXTURE EVOLUTION

The simulation of deformation textures in titanium alloys can be performed using a number of different approaches including the Taylor (isostrain) formulation;

viscoplastic, self-consistent (VPSC) analysis; and the crystal-plasticity, finite-element method (CPFEM).

Taylor Analysis

The Taylor analysis can be used for simulating the evolution of deformation texture for both single- and two-phase titanium alloys to various degrees of accuracy.

Single-Phase Beta Titanium. Glavicic, *et al.* [19] and Gey, *et al.* [48] demonstrated that a rate-sensitive Taylor-type model can be used to simulate beta-texture development during hot working of Ti-6Al-4V in the single-phase beta field. The former effort focused on texture evolution during the initial, beta-hot-working breakdown operations for production scale ingots. To this end, the local strains imparted to the workpiece were first estimated using a commercial “continuum” FEM code, DEFORM™ (Scientific Forming Technologies Corporation, Columbus, OH). The strain increments so determined were inserted in the Los Alamos polycrystalline plasticity (LApp) code [49] assuming deformation via slip on {110}<111> and {112}<111> systems. By this means, a <110> fiber texture was predicted for the billet center at which the initial (solidification) texture had been random. Model predictions showed good agreement with the experimental beta texture, whose determination required measurements of the alpha-phase texture due to the limited amount of beta phase for Ti-6Al-4V at room temperature [50, 51].

Gey, *et al.* [48] analyzed the rolling of Ti-6Al-4V plate in the beta phase field. They assumed the same slip systems as in the work of Glavicic, *et al*. [19], but chose a relaxed - constraints approach. That is to say, two of the three shear strains were not forced to be identical in all grains because of the pancake shape of the grains developed during rolling to heavy reductions. The simulated texture for a 75 pct. thickness reduction showed relatively good agreement with measurements (Figure 17). The major difference lay in the absolute intensity of texture components; the simulations showed stronger maxima compared to the observations. Such differences are common for crystal-plasticity models which typically neglect accommodation of the imposed deformation via dynamic-recovery/dislocation-climb processes.

Two-Phase Titanium Alloys. Taylor-type models can also be used to estimate the deformation textures developed in the individual phases during the hot working of two-phase titanium alloys with an equiaxed-alpha microstructure, such as occurs during alpha/beta forging or rolling of alpha/beta titanium alloys. One such approach is that developed by Glavicic, *et al.* [52] for the prediction of texture evolution during the hot pancake forging of Ti-6Al-4V. In this approach, a continuum FEM code is used first to estimate the "macroscopic" strains/strain increments and rigid-body rotations at each point of the workpiece. An approximate analysis is then used to estimate the partitioning of strain between the (harder) alpha phase particles and the (softer) beta phase matrix grains at specific points of interest. Next, a rate-sensitive Taylor analysis is applied to estimate the rotations associated with slip within each separate phase. Last, the rotations due to rigid-body motion (metal flow) and crystallographic slip are summed to determine the final texture of the alpha and beta phases.

To partition the strain between the alpha and beta phases, Glavicic, *et al.* [52] used an approximate self-consistent analysis for two-phase materials each of whose constituents has the same strain rate sensitivity m and a constitutive response of the form $\sigma_i = k_i \dot{\varepsilon}_i^m$; $\sigma(\dot{\varepsilon})$ and k_i denote the flow stress as a function of strain rate and the strength coefficient for the specific phase, respectively. The model was based on the approach developed by Hill [53] for linearly elastic solids, which was later extended to the case of rate-sensitive, incompressible materials by Suquet [54]. Subsequently, it was applied to titanium alloys by Briottet, *et al.* [55] and Semiatin, *et al.* [56]. The analysis leads to the determination of an effective strength coefficient k for the two-phase aggregate, whose overall constitutive response is assumed to be $\sigma = k\dot{\varepsilon}^m$. The strength coefficient k depends on the ratio of the strength coefficients of the two phases, k_a/k_β, and the volume fraction of the harder phase (alpha for the case of alpha/beta titanium alloys), i.e., f_α. Results of the analysis for m = 0.23 (i.e., the m for the alpha and beta phases of Ti-6Al-4V) are shown in Figure 18a. Results for m = 0.15 and m = 0.30 are similar.

The values of k_α and k_β depend on phase composition and temperature [56, 57]. An analysis of a large collection of flow stress data for various alloys has led to the finding that the ratio k_α/k_β for the alpha and beta phases in Ti-6Al-4V is almost constant at temperatures between 815 and 982°C and has a value of 3 [56].

The *average* strain rates in the alpha and beta phases (and hence the strain partitioning between the phases) are readily calculated from the values of k, k_α, k_β, and f_α by noting that the aggregate flow stress and strain rate are volume averages of the corresponding quantities for the components [58]. This leads to the following expressions for $\dot{\varepsilon}_\alpha / \dot{\varepsilon}_{ov}$ and $\dot{\varepsilon}_\beta / \dot{\varepsilon}_{ov}$, in which $\dot{\varepsilon}_{ov}$ is the overall (aggregate) strain rate:

$$k / k_\alpha = f_\alpha (\dot{\varepsilon}_\alpha / \dot{\varepsilon}_{ov})^m + [(1 - f_\alpha)^{(1-m)} (k_\beta / k_\alpha) \{1 - f_\alpha (\dot{\varepsilon}_\alpha / \dot{\varepsilon}_{ov})\}^m] \qquad (15a)$$

$$\dot{\varepsilon}_\beta / \dot{\varepsilon}_{ov} = [1 - f_\alpha (\dot{\varepsilon}_\alpha / \dot{\varepsilon}_{ov})] / (1 - f_\alpha) \qquad (15b)$$

Equation (15a) cannot be solved analytically, but is readily evaluated using numerical techniques leading to nomographs such as those in Figure 18b, c.

Using this approach for strain partitioning, Glavicic, *et al.* [52] applied the rate-sensitive Taylor code LApp to predict the deformation texture of the primary alpha phase at various locations in a pancake of Ti-6Al-4V forged at 955°C, i.e., ~40°C below the beta-transus temperature. The predictions showed reasonable qualitative agreement with measurements (Figure 19), but the magnitudes of the texture components were high, a trend similar to that discussed above with regard to the work of Gey, *et al.* [48].

VPSC and CPFEM Analyses

Viscoplastic self-consistent (VPSC) and crystal-plasticity FEM (CPFEM) approaches can also be used to model the evolution of deformation texture in two-phase titanium alloys. In the former approach, the strain is assumed to be homogeneous with each grain, but may vary from one grain/phase to another. The CPFEM technique enables strain variations *within* grains/phases as well as from grain to grain to be investigated. Details on these simulation techniques are contained in other articles in this volume. Hence, only some key results of such analyses are summarized here.

The VPSC analysis has been applied to alpha/beta titanium alloys with an equiaxed-alpha or a lamellar-colony microstructure. In the work of Dunst and Mecking [59], for example, texture evolution during the rolling of plate to a 70-pct. thickness reduction in a single pass at 800°C was investigated for a series of *equiaxed-alpha* alloys with different volume fractions of the two phases. Alloying was chosen so that the compositions of the alpha and beta phases were the same in each case. The evolution of deformation texture was simulated using the VPSC approach of Lebensohn and Tome [60]. Using a fitting procedure to get the best deformation texture predictions for *single-phase* alloys, the critical resolved shear stresses (CRSS) for slip were taken to be in the ratio of 1:1:1.5:3:1/3:1/3:1/3 for the four assumed alpha-phase systems (prism <a>, pyramidal <a>, basal <a>, pyramidal <c+a>) and the three assumed beta-phase systems ({110}<111>, {112}<110>, and {123}<110>). The strain-rate sensitivity (m) was set at 0.2 for both phases.

Alpha-phase textures predicted by Dunst and Mecking using the VPSC approach showed good agreement with measurements (Figure 20). The calculated activity of different slip systems and microstructure observations revealed that “hard” alpha-grain orientations (i.e., those whose c axes lay in the plate normal direction) tended to remain undeformed as the volume fraction of alpha decreased. On the other hand, soft alpha grains deformed predominantly by single slip (along prism <a> systems) as the alpha volume fraction increased; the strain incompatibility was accommodated by the deformation of the beta phase. Predicted beta-phase textures showed poorer agreement with measurements, an effect ascribed to local interactions between the beta and alpha phases which were not treated in the VPSC model.

Deformation texture development in alpha/beta titanium alloys with a *colony-alpha* microstructure can also be described using a VPSC approach [61]. The best alpha-phase predictions are obtained when the “correlation” between alpha lamellae and the beta matrix (i.e., the Burgers relation between the phases *and* an alpha-beta interface close to a prism plane in the alpha phase) is taken into consideration. Local interactions and non-uniform local flow of the beta phase make the prediction of beta deformation textures somewhat problematical as in VPSC simulations for equiaxed microstructures, however.

CPFEM simulations can also be used to quantify strain partitioning and texture evolution in two-phase titanium alloys. For example, Turner and Semiatin [61] examined the effect of the degree of microstructure discretization on strain partitioning between a hard and a soft phase. Predictions were found to differ noticeably for so-called meso-scale and micro-scale modeling approaches. For the former, each grain is represented by a single element in the CPFEM simulation, whereas each grain is divided into multiple elements for micro-scale simulations. The higher level of discretization produces predictions of strain partitioning similar to those from the approximate self-consistent model of Suquet, Semiatin, and their co-workers [54, 56] (Figure 21a).

The usefulness of CPFEM to quantify local deformation and texture evolution for two-phase alpha/beta titanium alloys has been demonstrated by Barton and Dawson [63]. In this work, the hot rolling of plate in which the volume fractions of the alpha and beta phases were varied was simulated; because of excessive mesh distortions, the thickness reduction was limited to 25 pct. The values of CRSS were similar to those used in the VPSC simulations of Dunst and Mecking [59]. As for other modeling approaches, the partitioning of strain between the alpha and beta phases is predicted by CPFEM to increase with a decrease in the volume fraction of the harder alpha phase (Figure 21b). Furthermore, non-negligible shear strain components can be quantified in CPFEM simulations. In the work of Barton and Dawson [63], it was shown that the shear strains tend to be higher in the beta phase and increase in magnitude with an increase in the volume fraction of alpha, thus underlining the need to quantify local neighborhood effects on texture evolution in the beta phase. In a similar vein, CPFEM simulations reveal that strain localization tends to occur in materials with roughly equal amounts of alpha and beta or slightly beta-rich alloys. In titanium alloys with a large volume fraction of beta, on the other hand, the alpha particles tend to undergo little deformation (but may experience noticeable rotations), and thus they are essentially carried along with the plastic flow of the beta. Textures predicted by CPFEM mirror measured ones, but limitations on the reduction level that can be simulated (due to excessive mesh distortion) preclude quantitative comparisons. Current and future increases in computing power are now overcoming such limitations for CPFEM simulations of texture evolution.

TRANSFORMATION TEXTURE EVOLUTION

The decomposition of the high-temperature metastable bcc beta phase during cooling often results in the preferential selection of a subset of the 12 possible hcp lamellar-alpha variants. This effect has been investigated most often for alpha/beta titanium alloys such as Ti-6Al-4V, and various approaches have been proposed to interpret observations for both heat-treating and deformation processes.

In the area of heat treatment, it has been found that variant selection tends to be weak for cold- or hot-rolled Ti-6Al-4V plate which is beta annealed and slow cooled [64, 65]. By contrast, a strong variant-selection process can occur for this material during rapid cooling from a heat treatment in the alpha + beta phase field [64]. For example, an analysis of the data of Moustahfid, *et al.* [64] by Divinski, *et al.* [66] suggests that the orientation of the beta-phase plane relative to the rolling plane controls the variants that are formed. In particular, good agreement between measured and predicted pole figures (Figure 22) is obtained when only one-half of the possible variants are chosen for each of the two principal beta-texture components ($\{112\}<1\bar{1}0>$ and $\{111\}<11\bar{2}>$, in which the two indices refers to the crystallographic plane/direction parallel to the rolling plane/rolling direction). It has been hypothesized that local stresses developed in two-phase material during cooling (as a result of differences in coefficients of thermal expansion) tend to favor the formation of alpha variants whose orientation is similar to that of the primary alpha [66].

When beta-phase decomposition follows hot deformation in the beta field, noticeable variant selection tends to occur [48]. In such cases, the selected alpha variants tend to correlate with the beta slip systems which have been most active during the prior deformation. The plausibility of this approach was demonstrated by Gey, *et al.* [67] for beta hot working via plate rolling. As described in the section on the modeling of deformation texture, the relative slip activity in the beta phase can be estimated using a Taylor-type model assuming deformation on {110}<111> and {112}<111> systems. Alpha variants may be presumed to nucleate on highly active {110}<111> beta-phase systems because of the direct Burgers orientation relation between the close-packed planes and directions in the two phases. In addition, Burgers [9] suggested that the beta-to-alpha transformation begins with shear movements of atoms on {112} planes in <111> directions. Thus, prior activity of specific {112}<111> systems may also favor the formation of related alpha variants. In the specific work of Gey, *et al.* [67], therefore, the volume fractions of alpha variants for each beta crystal orientation were assigned in direct proportion to the relative activity on those slip systems that underwent a certain minimum shear strain; the minimum was taken to be 50 pct. of the maximum shear strain for the particular crystal orientation. With a variant-selection rule of this form, texture predictions in good agreement with observation can be made (Figure 23).

An alternate, but related, variant selection rule for the decomposition of hot-worked beta has been proposed and validated by Moustahfid, *et al.* [68]. This alternate rule chooses among the various possible {110}<111> and {112}<111> slip systems for each crystal orientation based on their relative Schmid factors/resolved shear stresses. Those systems whose Schmid factors are within 10 pct. of the maximum Schmid factor are assumed to form an alpha variant.

FUTURE OUTLOOK

The current status of the modeling and simulation of the evolution of crystallographic texture in titanium and titanium alloys due to recrystallization, grain growth, deformation, and phase transformation has been summarized. For these materials, the development of a fundamental understanding of texture formation tends to be challenging from an experimental standpoint because of the high temperatures involved in typical industrial processes and the allotropic transformation of many alloys of commercial interest. Hence, modeling and simulation provide useful tools for phenomena that are not easily observed. Recent developments in this area underscore the coupled nature of the evolution of texture and microstructure and the need to treat both aspects in realistic physics-based models. Important areas of future development include the following:

- Development of databases of material properties needed for simulations. These properties include grain-boundary energy and mobility and stress-strain-strain-rate constitutive behavior at large strains for slip in both alpha and beta titanium.
- The development of an understanding of the effect of strain path on large-strain constitutive behavior at the crystal scale.
- Incorporation of recovery in deformation-texture models.
- Development of variant selection rules to describe the decomposition of beta during cooling following heat treatment or hot working, especially for alpha/beta titanium alloys processed in the two-phase field.

Acknowledgements- A large portion of this article evolved from efforts championed and supported over many years by the management of the Materials and Manufacturing Directorate and the Air Force Office of Scientific Research of the Air Force Research Laboratory. Technical discussions with our colleagues are very much appreciated.

REFERENCES

1. U.F. Kocks, C.N. Tome, and H.R. Wenk, *Texture and Anisotropy*, Cambridge University Press, Cambridge, UK, 1998.
2. C.N. Tome and A.J. Beaudoin, “Polycrystal Modeling, Plastic Forming, and Deformation Textures,” *ASM Handbook, Volume 14A, Metalworking: Bulk Forming*, ASM International, Materials Park, OH, 2005, pp.671-684.
3. L. Kestens and J.J. Jonas, “Transformation and Recrystallization Textures associated with Steel Processing,” *ASM Handbook, Volume 14A, Metalworking: Bulk Forming*, ASM International, Materials Park, OH, 2005, pp.685-700.

4. F. Larson and A. Zarkades “Properties of Textured Titanium Alloys,” Report MCIC-74-20, Metals and Ceramics Information Center, Battelle's Columbus Laboratories, Columbus, OH, 1974.
5. G. Lütjering and M. Peters, “Mechanical Properties of a Titanium Blading Alloy,” Report EPRI-CS-2933, Electric Power Research Institute, Palo Alto, CA, 1983.
6. G. Lütjering and J.C. Williams, *Titanium*: Springer Verlag, Berlin, 2007.
7. I. Weiss and S.L. Semiatin, "Thermomechanical Processing of Beta Titanium Alloys - An Overview," *Mat. Sci. Eng.A*, 1998, vol. A243, pp. 46-65.
8. I. Weiss and S.L. Semiatin, "Thermomechanical Processing of Alpha Titanium Alloys - An Overview," *Mater. Sci. Eng. A*, 1999, vol. A263, pp. 243-256.
9. W.G. Burgers, ”On the Process of Transition of the BCC Modification into the HCP Modification of Zirconium,” *Physica*, 1934, vol. 1, pp. 561-586.
10. B. Hutchinson and B. Wynne, “Effects of Stress on Structure Transformations in Metals,” *Mater. Sci. Forum*. 2007, vol. 550, pp. 149-158.
11. V. Randle and O. Engler, *Introduction to Texture Analysis: Macrotexture, Microtexture, and Mapping*, Taylor & Francis Ltd, London, 2000.
12. H.J. Bunge, *Texture Analysis in Materials Science*, Butterworths, Boston, 1982.
13. A.A. Salem, S.R. Kalidindi, and R.D. Doherty, “Strain Hardening of Titanium: Role of Deformation Twinning,” *Acta Mater.*, 2003, vol. 51, pp. 4225-4237.
14. Y.B. Chun, S.H. Yu, S.L. Semiatin, and S.K. Hwang, “Effect of Deformation Twinning on Microstructure and Texture Evolution during Cold Rolling of CP Titanium,” *Mater. Sci. Eng. A*, 2005, vol. A398, pp. 209-219.

15. S.L. Semiatin and T.R. Bieler, “Effect of Texture and Slip Mode on the Anisotropy of Plastic Flow and Flow Softening during Hot Working of Ti-6Al-4V,” *Metall. Mater. Trans. A*, 2001, vol. 32A, pp. 1787- 1799.
16. H.R. Piehler and W.A. Backofen, “A Theoretical Examination of the Plastic Properties of BCC Crystals Deforming by <111> Pencil Glide,” *Metall. Trans.*, 1971, vol. 2, pp. 249-255.
17. P.R. Morris and S.L. Semiatin, “The Prediction of Plastic Properties of Polycrystalline Aggregates of BCC Metals Deforming by <111> Pencil Glide,” *Texture of Crystalline Solids*, 1979, vol. 3, pp. 113-126.
18. G.Y. Chin and W.L. Mammel, “Computer Solutions of the Taylor Analysis for Axisymmetric Flow,” *Trans. AIME*, 1967, vol. 239, pp. 1400-1405
19. M.G. Glavicic, P.A. Kobryn, R.L. Goetz, K.O. Yu, and S.L. Semiatin, “Texture Evolution during Primary Processing of Production-Scale Vacuum-Arc-Remelted Ingots of Ti-6Al-4V,” *Ti-2003: Science and Technology*, G. Lütjering and J. Albrecht, eds., Wiley-VCH GmbH, Weinheim, Germany, 2004, pp. 1299-1306.
20. W. Pichl, “Slip Geometry and Plastic Anisotropy of Body-Centered Cubic Metals,” *Physica Status Solidi (a)*, 2002, vol. 189, pp. 5-25.
21. S.P. Fox, “A Study of Grain-Growth Behavior in Titanium Alloys,” *Titanium ’92: Science and Technology*, F.H. Froes and I.L. Caplan, eds., TMS, Warrendale, PA, 1992, pp. 769 – 776.
22. O.M. Ivasishin, S.V. Shevchenko, and S.L. Semiatin, “Effect of Crystallographic Texture on the Isothermal Beta Grain-Growth Kinetics of Ti-6Al-4V,” *Mater. Sci. Eng. A*, 2002, vol. A332, pp. 343-350.

23. O.M. Ivasishin, S.L. Semiatin, P.E. Markovsky, S.V. Shevchenko, and S.V. Ulshin, "Grain Growth and Texture Evolution in Ti-6Al-4V during Beta Annealing under Continuous Heating Conditions," *Mater. Sci. Eng. A*, 2002, vol. A337, pp. 88-96.

24. O.M. Ivasishin, S.V. Shevchenko, P.E. Markovsky, and S.L. Semiatin, "Experimental Investigation and 3D Monte-Carlo Simulation of Texture-Controlled Grain Growth in Titanium Alloys," *Ti-2003: Science and Technology*, G. Lütjering and J. Albrecht, eds., Wiley-VCH GmbH, Weinheim, 2004, pp. 1307-1314.

25. O.M. Ivasishin, S.V. Shevchenko, N.L. Vasiliev, and S.L. Semiatin, "3D Monte-Carlo Simulation of Texture-Controlled Grain Growth," *Acta Mater.*, 2003, vol. 51, pp. 1019-1034.

26. G. Abbruzzese and K. Lücke, "A Theory of Texture Controlled Grain Growth – Derivation and General Discussion of the Model," *Acta Metall.*, 1986, vol. 34, 1986, pp. 905-914.

27. H. Eichelkraut, G. Abbruzzese, and K. Lücke, "A Theory of Texture-Controlled Grain Growth – II. Numerical and Analytical Treatment of Grain Growth in the Presence of Two Texture Components ," *Acta Metall.*, 1988, vol. 36, pp. 55-68.

28. O.M. Ivasishin, S.V. Shevchenko, and S.L. Semiatin, "Implementation of Exact Grain-Boundary Geometry into a 3D Monte-Carlo (Potts) Model for Microstructure," submitted to *Acta. Mater.*, 2008.

29. G. Gottstein and L.S. Shvindlerman, *Grain-Boundary Migration in Metals*, CRC Press, Boca Raton, Florida, 1999.

30. Y. Amouyal, E. Rabkin, and Y. Mishin, "Correlation between Grain-Boundary Energy and Geometry in Ni-Rich NiAl," *Acta Mater.*, 2005, vol. 53, pp. 3795-3805.

31. N. Ma and Y. Wang, “Beta Grain-Growth Kinetics in Ti-6Al-4V,” *Numiform 2004*, S. Ghosh, J.M. Castro, and J.K. Lee, eds., American Institute of Physics, College Park, Maryland, 2004, pp. 1700-1704

32. N. Ma, A. Kazaryan, S.A. Dregia, and Y. Wang, “Computer Simulation of Texture Evolution during Grain Growth: Effect of Boundary Properties and Initial Microstructure,” *Acta Mater.*, 2004, vol. 52, pp. 3869-3879.

33. I. Weiss and F.H. Froes, "The Processing Window for the Near Beta Ti-10V-2Fe-3Al Alloy,” *Titanium: Science and Technology*, G. Lütjering, U. Zwicker, and W. Bunk, eds., Deutsche Gesellschaft für Metallkunde e.V., Oberursel, Germany, 1985, pp. 499-506.

34. O.M. Ivasishin, S.V. Shevchenko, N.L. Vasiliev, and S.L. Semiatin, “A 3-D Monte-Carlo (Potts) Model for Recrystallization and Grain Growth in Polycrystalline Materials,” *Mater. Sci. Eng. A*, 2006, vol. A433, pp. 216-232.

35. R. Ding and Z.X. Guo, “Microstructural Modelling of Dynamic Recrystallization Using an Extended Cellular Automaton Approach,” *Comp. Mater. Sci.*, 2002, vol. 23, pp. 209-218.

36. R. Ding and Z.X. Guo, “Microstructural Evolution of a Ti-6Al-4V Alloy during Beta-Phase Processing: Experimental and Simulative Investigations,” *Mater. Sci. Eng. A*, 2004, vol. A365, pp. 172-179.

37. A.D. Rollett and E.A. Holm, “Abnormal Grain Growth – The origin of Recrystallization Nuclei?,” *ReX’96, Proceedings of the Third International Conference on Recrystallization and Related Phenomena*, T.R. McNelley, ed., Monterey Institute of Advanced Studies, Monterey, CA, 1997, pp. 31-42.

38. R.D. Doherty, D.A. Hughes, F.J. Humphreys, J.J. Jonas, D. Jul Jensen, M.E. Kassner, W.E. King, T.R. McNelly, H.J. McQueen, A.D. Rollett, "Current Issues in Recrystallization: A Review," *Mater. Sci. Eng. A*, 1997, vol. A238, pp. 219-274.

39. B. Radhakrishnan, G.B. Sarma, and T. Zacharia, "Modeling the Kinetics and Microstructure Evolution during Static Recrystallization – Monte-Carlo Simulation of Recrystallization," *Acta Mater.*, 1998, vol. 46, pp. 4415-4433.

40. Y.B. Chun, S.L. Semiatin, and S.K. Hwang, "Role of Deformation Twinning in Cold Rolling and Recrystallization of Titanium," *Mater. Sci. Forum*, 2005, vols. 495-497, pp. 651-656.

41. Y.B. Chun and S.K. Hwang, "Static Recrystallization of Warm-Rolled Pure Titanium Influenced by Microstructural Inhomogeneity," *Acta Mater.*, 2008, vol. 56, pp. 369-379.

42. Y.B. Chun, S.L. Semiatin, and S.K. Hwang, "Monte-Carlo Modeling of Microstructure Evolution during the Static Recrystallization of Cold-Rolled, Commercial-Purity Titanium," *Acta Mater.*, 2006, vol. 54, pp. 3673-3689.

43. D.E. Solas, C.N. Tomé, O. Engler, and H.R. Wenk, "Deformation and Recrystallization of Hexagonal Metals: Modeling and Experimental Results for Zinc," *Acta Mater.*, 2001, vol. 49, pp. 3791-3801.

44. F. Caleyo, T. Baudin, and R. Penelle, "Monte-Carlo Simulation of Recrystallization in Fe-50 Pct. Ni Starting from EBSD and Bulk Texture Measurements," *Scripta Mater.*, 2002, vol. 46, pp. 829-835.

45. S.H. Choi and J.H. Cho, "Primary Recrystallization Modeling for Interstitial-Free Steels," *Mater. Sci. Eng. A*, 2005, vol. A405, pp. 86-101.

46. F.J. Humphreys and M. Hatherly, *Recrystallization and Related Annealing Phenomena*, Elsevier Science Ltd., Oxford, UK, 1996.

47. J.W. Cahn and W. Hagel, “Theory of the Pearlite Reaction”, *Decomposition of Austenite by Diffusional Processes*, V.F. Zackay and H.I. Aaronson, eds., Interscience, New York, 1960, pp. 131-196.

48. N. Gey, M. Humbert, M.J. Philippe, and Y. Combres, “Investigation of the Alpha- and Beta- Texture Evolution of Hot Rolled Ti-64 Products,” *Mater. Sci. Eng. A*, 1996, vol. A219, pp. 80-88.

49. Los Alamos Polycrystal Plasticity Code, Los Alamos National Laboratory report LA-CC-88-6, Los Alamos, NM, 1988.

50. M. Humbert, H. Moustahfid, F. Wagner, and M.J. Philippe, “Evaluation of the High-Temperature Texture of the Beta Phase of a Ti-6Al-4V Sample from the Individual Orientations of Grains of the Low-Temperature Alpha Phase,” *Scripta Metall. et Mater.*, 1994, vol. 30, pp. 377-382.

51. M.G. Glavicic, P.A. Kobryn, T.R. Bieler, and S.L. Semiatin, “A Method to Determine the Orientation of the High-Temperature Beta Phase from Measured EBSD Data for the Low-Temperature Alpha Phase in Ti-6Al-4V,” *Mater. Sci. Eng. A*, 2003, vol. A346, pp. 50-59.

52. M.G. Glavicic, R.L. Goetz, D.R. Barker, G. Shen, D. Furrer, A. Woodfield, and S.L. Semiatin, “Modeling of Texture Evolution during Hot Forging of Alpha/Beta Titanium Alloys,” *Metall. Mater. Trans. A*, 2008, vol. 39A, pp. 887-896.

53. R. Hill, “A Self-Consistent Mechanics of Composite Materials,” *J. Mech. Phys. Solids*, 1965, vol. 13, pp. 213-222.

54. P.M. Suquet, “Overall Potentials and External Surfaces of Power Law or Ideally Plastic Composites,” *J. Mech. Phys. Solids*, 1993, vol. 41, pp. 981-1002.

55. L. Briottet, J.J. Jonas, and F. Montheillet, “A Mechanical Interpretation of the Activation Energy of High-Temperature Deformation in Two-Phase Materials,” *Acta Mater*., 1996, vol. 44, pp. 1665-1672.

56. S.L. Semiatin, F. Montheillet, G. Shen, and J.J. Jonas, “Self-Consistent Modeling of the Flow Behavior of Wrought Alpha/Beta Titanium Alloys under Isothermal and Nonisothermal Hot-Working Conditions,” *Metall. Mater. Trans. A*, 2002, vol. 33A, pp. 2719-2727

57. P. Vo, M. Jahazi, S. Yue, and P. Bocher, “Flow Stress Prediction during Hot Working of Near-Alpha Titanium Alloys,” *Mater. Sci. Eng. A*, 2007, vol. A447, pp. 99-110.

58. R. Hill, “The Essential Structure of Constitutive Laws for Metal Composites and Polycrystals,” *J. Mech. Phys. Solids*, 1967, vol. 15, pp. 79-95.

59. D. Dunst and H. Mecking, “Analysis of Experimental and Theoretical Rolling Textures of Two-Phase Titanium Alloys,” *Zeitschrift für Metallkunde*, 1996, vol. 87, pp. 498-507.

60. R. Lebensohn and C. Tomé, “A Self-Consistent Anisotropic Approach for the Simulation of Plastic Deformation and Texture Development of Polycrystals: Application to Zirconium Alloys,” *Acta Metall. Mater.*, 1993, vol. 41, pp. 2611-2624.

61. R.A. Lebensohn and G.R. Canova, “A Self-Consistent Approach for Modelling Texture Development of Two-Phase Polycrystals: Application to Titanium Alloys,” *Acta Mater.*, 1997, vol. 45, pp. 3687-3694.

62. T.J. Turner and S.L. Semiatin, "A Crystal-Plasticity Model for the Flow behavior of Two-Phase Alloy Systems," *Numiform 2004*, S. Ghosh, J.M. Castro, and J.K. Lee, eds., American Institute of Physics, College Park, Maryland, 2004, pp. 1792-1797.

63. N.R. Barton and P.R. Dawson, "On the Spatial Arrangement of Lattice Orientation in Hot-Rolled Multiphase Titanium," *Model. Simul. Mater. Sci. Eng.*, 2001, vol. 9, pp. 433-463.

64. H. Moustahfid, N. Gey, M. Humbert, and M.J. Philippe, "Study of the Beta-Alpha Phase Transformations of a Ti-64 Sheet Induced from a High-Temperature Beta State and a High-Temperature Alpha+Beta State," *Metall. Mater. Trans. A*, 1997, vol. 28A, pp. 51-59.

65. M.G. Glavicic, P.A. Kobryn, T.R. Bieler, and S.L. Semiatin, "An Automated Method to Determine the Orientation of the High-Temperature Beta Phase from Measured EBSD Data for the Low-Temperature Alpha-Phase in Ti-6Al-4V," *Mater. Sci. Eng. A*, 2003, vol. A351, pp. 258-264.

66. S.V. Divinski, V.N. Dnieprenko, and O.M. Ivasishin, "Effect of Phase Transformation on Texture Formation Ti-Base Alloys," *Mater. Sci. Eng. A*, 1998, vol. A243, pp. 201-205.

67. N. Gey, M. Humbert, M.J. Philippe, and Y. Combres, "Modeling the Transformation Texture of Ti-64 Sheets after Rolling in the Beta Field," *Mater. Sci. Eng. A*, 1997, vol. A230, pp. 68-74.

68. H. Moustahfid, M. Humbert, and M.J. Philippe, "Modeling of the Texture Transformation in a Ti-64 Sheet after Hot Compression," *Acta Mater.*, 1997, vol. 45, pp. 3785-3790.

Table I. Miller-Index Equivalents for HCP Slip Systems in an Orthogonal Coordinate System [15]

Slip System	HCP Indices	Equivalent Indices in Cubic Coordinates
Basal $\langle a \rangle$	$(0001)\ [2\bar{1}\bar{1}0]$	$(001)\ [1\ 0\ 0]$
Basal $\langle a \rangle$	$(0001)\ [\bar{1}2\bar{1}0]$	$(001)\ [-1/2\ \sqrt{3}/2\ 0]$
Basal $\langle a \rangle$	$(0001)\ [\bar{1}\bar{1}20]$	$(001)\ [-1/2\ -\sqrt{3}/2\ 0]$
Prism $\langle a \rangle$	$(10\bar{1}0)\ [\bar{1}2\bar{1}0]$	$(\sqrt{3}/2\ 1/2\ 0)\ [-1/2\ \sqrt{3}/2\ 0]$
Prism $\langle a \rangle$	$(1\bar{1}00)\ [\bar{1}\bar{1}20]$	$(\sqrt{3}/2\ -1/2\ 0)\ [-1/2\ -\sqrt{3}/2\ 0]$
Prism $\langle a \rangle$	$(01\bar{1}0)\ [2\bar{1}\bar{1}0]$	$(0\ 1\ 0)\ [1\ 0\ 0]$
Pyramidal $\langle a \rangle$	$(10\bar{1}1)\ [\bar{1}2\bar{1}0]$	$(1\ 1/\sqrt{3}\ 1/\rho)\ [-1/2\ \sqrt{3}/2\ 0]$
Pyramidal $\langle a \rangle$	$(\bar{1}011)\ [\bar{1}2\bar{1}0]$	$(-1\ -1/\sqrt{3}\ 1/\rho)\ [-1/2\ \sqrt{3}/2\ 0]$
Pyramidal $\langle a \rangle$	$(01\bar{1}1)\ [2\bar{1}\bar{1}0]$	$(0\ 2/\sqrt{3}\ 1/\rho)\ [1\ 0\ 0]$
Pyramidal $\langle a \rangle$	$(0\bar{1}11)\ [2\bar{1}\bar{1}0]$	$(0\ -2/\sqrt{3}\ 1/\rho)\ [1\ 0\ 0]$
Pyramidal $\langle a \rangle$	$(1\bar{1}01)\ [\bar{1}\bar{1}20]$	$(1\ -1/\sqrt{3}\ 1/\rho)\ [-1/2\ -\sqrt{3}/2\ 0]$
Pyramidal $\langle a \rangle$	$(\bar{1}101)\ [\bar{1}\bar{1}20]$	$(-1\ 1/\sqrt{3}\ 1/\rho)\ [-1/2\ -\sqrt{3}/2\ 0]$
Pyramidal $\langle c + a \rangle$	$(10\bar{1}1)\ [a_1 - c],\ [-a_3 - c]$	$(1\ 1/\sqrt{3}\ 1/\rho)\ [1\ 0\ -\rho],\ [1/2\ \sqrt{3}/2\ -\rho]$
Pyramidal $\langle c + a \rangle$	$(\bar{1}011)\ [-a_1 - c],\ [a_3 - c]$	$(-1\ -1/\sqrt{3}\ 1/\rho)\ [-1\ 0\ -\rho],\ [-1/2\ -\sqrt{3}/2\ -\rho]$
Pyramidal $\langle c + a \rangle$	$(01\bar{1}1)\ [a_2 - c],\ [-a_3 - c]$	$(0\ 2/\sqrt{3}\ 1/\rho)\ [-1/2\ \sqrt{3}/2\ -\rho],\ [1/2\ \sqrt{3}/2\ -\rho]$
Pyramidal $\langle c + a \rangle$	$(0\bar{1}11)\ [-a_2 - c],\ [a_3 - c]$	$(0\ -2/\sqrt{3}\ 1/\rho)\ [1/2\ -\sqrt{3}/2\ -\rho],\ [-1/2\ -\sqrt{3}/2\ -\rho]$
Pyramidal $\langle c + a \rangle$	$(1\bar{1}01)\ [a_1 - c],\ [-a_2 - c]$	$(1\ -1/\sqrt{3}\ 1/\rho)\ [1\ 0\ -\rho],\ [1/2\ -\sqrt{3}/2\ -\rho]$
Pyramidal $\langle c + a \rangle$	$(\bar{1}101)\ [-a_1 - c],\ [a_2 - c]$	$(-1\ 1/\sqrt{3}\ 1/\rho)\ [-1\ 0\ -\rho],\ [-1/2\ \sqrt{3}/2\ -\rho]$
$\rho \equiv c/a = 1.59$		

Figure Captions

Figure 1. Close-packed planes/directions and crystallography of (a) hcp alpha titanium and (b) bcc beta titanium. The Burgers orientation relation between the beta and one of the 12 possible alpha variants is shown in (c).

Figure 2. Orientation relation between the orthogonal sample reference directions and the orthogonal crystal reference directions: (a) Geometry in terms of angles between the two systems of axes (for clarity, only the angles α_1, β_1, and γ_1 are shown) and (b) Euler angles using the Bunge convention [11].

Figure 3. Common slip systems for hcp (alpha) titanium crystals: (a) basal <a>, (b) prism <a>, and (c) pyramidal <c+a>.

Figure 4. Observations of beta grain-growth in Ti-6Al-4V sheet with a strong initial texture, showing periods of rapid and slow growth [22].

Figure 5. Monte-Carlo model simulation of texture-controlled grain growth for a material with two texture components: (a) Comparison of predicted grain-growth kinetics (solid line) and normal grain-growth kinetics (broken line) and (b) simulated (100) pole figures after various times. MU ~ model lattice units, MCS ~ Monte-Carlo steps. In (b), the iso-intensity lines correspond to 1, 2, 5, 10, and >30 times random, and the 010 and 001 poles are not shown for clarity. [25]

Figure 6. Monte-Carlo model predictions of the grain-size distributions after 15 Monte-Carlo steps for the simulation of texture-controlled grain growth in a material with two texture components: (a) For the entire material and (b) for the grains belonging to texture component A. MU ~ model lattice units. [25]

Figure 7. Predictions of the volume fraction of the texture components and the grain size as a function of annealing time for a two-component initial texture using: (a) an MC method [25] and (b) an analytical approach [27]. The labels for components A and B in (b) have been switched from those in Reference 27 in order to coincide with the nomenclature in Reference 25.

Figure 8. Baseline dependences of (a) grain-boundary energy and mobility (m_a =1) on misorientation and (b) stored-energy on location used in MC simulations of recrystallization and grain growth [34].

Figure 9. MC simulation predictions of the effect of initial stored-energy distribution on recrystallization, assuming randomly-oriented nuclei: (a) Recrystallized fraction X and (b) corresponding Avrami plots [34]. The letters in the figures refer to the stored-energy distributions shown in Figure 8b.

Figure 10. MC-predicted dependence of microstructure evolution in an initially wrought material (shown in (a)) after 100 MCS assuming identical nuclei orientations and a mobility of the special boundaries which was (b) the same or (c) 40 pct. higher than that of other non-special high-angle boundaries [34].

Figure 11. Microstructures developed during cold rolling of CP titanium to a thickness reduction of (a) 20 pct. or (b) 60 pct. Figure (c) shows an EBSD image-quality map for material cold-rolled to a 60-pct. reduction. The rolling direction is horizontal, and the sheet normal direction is vertical in all micrographs. [14, 40, 42]

Figure 12. Pole figures for CP titanium cold rolled to percent thickness reductions of (a) 0, (b) 40, and (c) 60 [14]. The maximum x-random texture intensities were

(a) 4.4. (b) 3.9, and (c) 3.7. The contour levels for all pole figures are 1.5, 2.0, 2.5,…7.5.

Figure 13. Static recrystallization behavior of CP titanium rolled to a thickness reduction of 60 pct. and annealed at 600°C: (a) Measured recrystallization kinetics, (b) the corresponding experimental Avrami plot, and (c) predicted kinetics from an MC simulation [42].

Figure 14. MC predictions of the dependence on recrystallized fraction X of the average velocity (V_{CH}) and total length per unit area (L_A) of the recrystallization front and the rate of recrystallization ($\Delta X/\Delta MCS$) for (1) the classical JMAK condition and (b) a condition involving recovery, heterogeneous nucleation at sites of high stored energy, and anisotropic grain-boundary properties [42].

Figure 15. Comparison of (a) experimental observations and (b) MC predictions of microstructure evolution during recrystallization of CP titanium cold-rolled to a 60-pct. thickness reduction and then annealed at 600°C [42].

Figure 16. Comparison of (a) measured and (b) MC-predicted textures developed during recrystallization of CP titanium cold-rolled to a 60-pct. thickness reduction and then annealed at 600°C. In both (a) and (b), the ODF on the top is for the as-deformed condition, and that on the bottom is for the fully recrystallized condition [42].

Figure 17. Comparison of (a) measured and (b) predicted (100) beta-phase pole figures for Ti-6Al-4V plate hot rolled to a 75-pct. thickness reduction in the beta phase field [48].

Figure 18. Predictions from an approximate self-consistent model for strain partitioning in a two-phase material with a rate sensitivity of 0.23. The graphs show the dependence on the ratio k_α/k_β and the volume fraction of the harder phase f_α of (a) the aggregate strength coefficient k and (b, c) the strain rates in the harder phase ($\dot{\varepsilon}_\alpha$) and softer phase($\dot{\varepsilon}_\beta$) relative to the overall (aggregate) strain rate($\dot{\varepsilon}_{ov}$) [56].

Figure 19. Comparison of the deformation texture (in terms of (0001) pole figures) developed in the primary alpha phase at the corner location of a Ti-6Al-4V billet which was pancake forged at 955°C: (a) measured and (b) predicted [52].

Figure 20. Comparison of (a-d) measured and (e-h) simulated alpha-phase (0001) pole figures for heavily-rolled titanium alloys having alpha/beta volume fractions (in pct.) of (a, e) 96/4, (b, f) 78/22, (c, g) 36/64, and (d, h) 18/82 [59].

Figure 21. Strain partitioning in two-phase alloys: (a) Comparison of CPFEM meso-scale and micro-scale model predictions with those from a self-consistent model [62] and (b) CPFEM predictions of the strain components in the alpha and beta phases during rolling of titanium plate with two different volume-fraction ratios [63].

Figure 22. Comparison of (0001) alpha-phase pole figures for Ti-6Al-4V plate that was heat treated high in the alpha + beta phase field and then rapidly cooled: (a) Measured [64], (b) predicted assuming random variant selection [66], and (c) predicted assuming biased variant selection [66].

Figure 23. Comparison of (0001) pole figures for colony-alpha formed during cooling following hot rolling of Ti-6Al-4V plate to a 75-pct. thickness reduction in the beta-phase field: (a) Measured and (b) predicted using a Taylor-type crystal-plasticity model and alpha-variant selection based on relative slip-system activity [67].

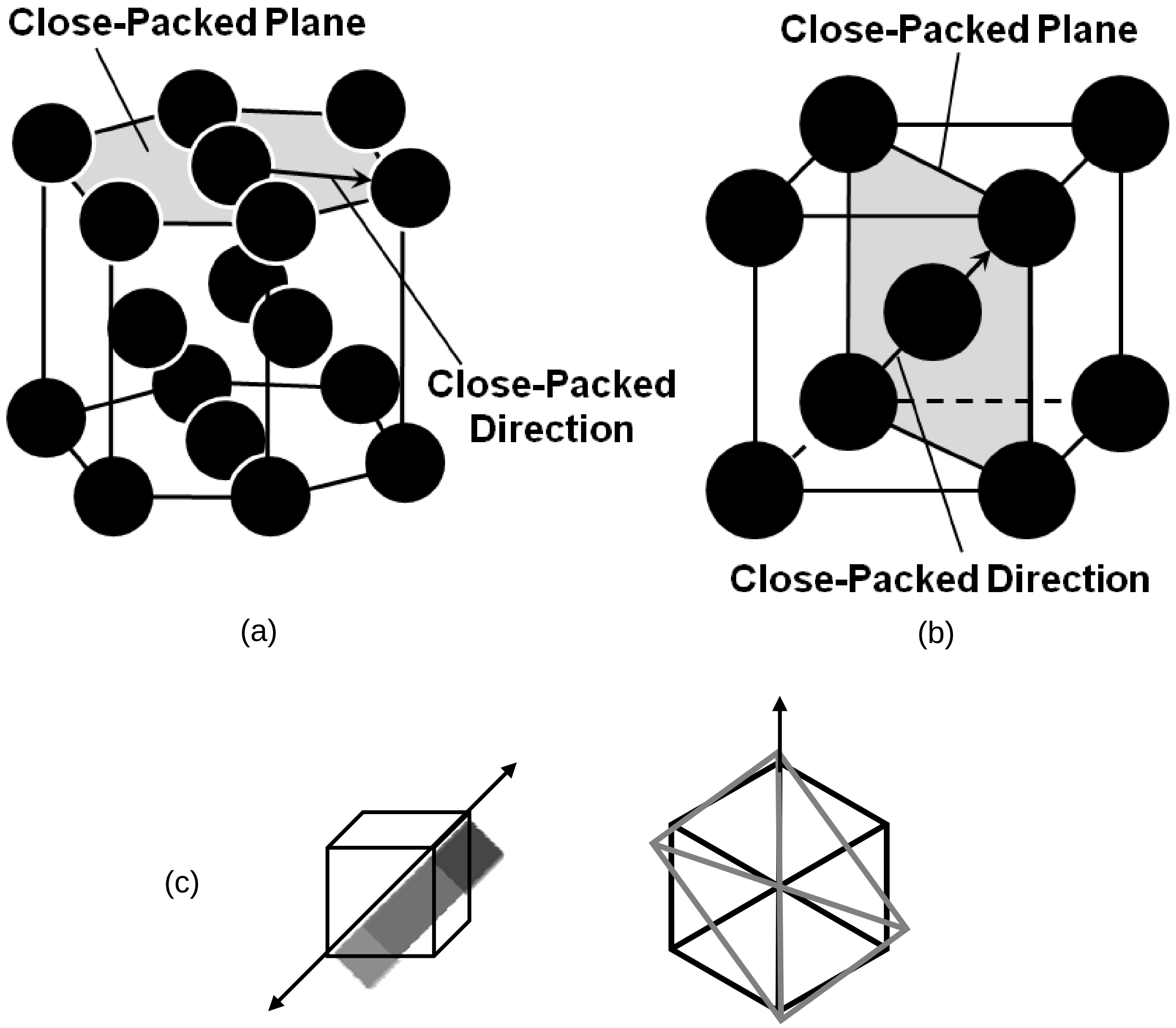
Close-Packed Plane
Close-Packed Direction
Close-Packed Plane
Close-Packed Direction

(a) (b)

(c)

Figure 1. Close-packed planes/directions and crystallography of (a) hcp alpha titanium and (b) bcc beta titanium. The Burgers orientation relation between the beta and one of the 12 possible alpha variants is shown in (c).

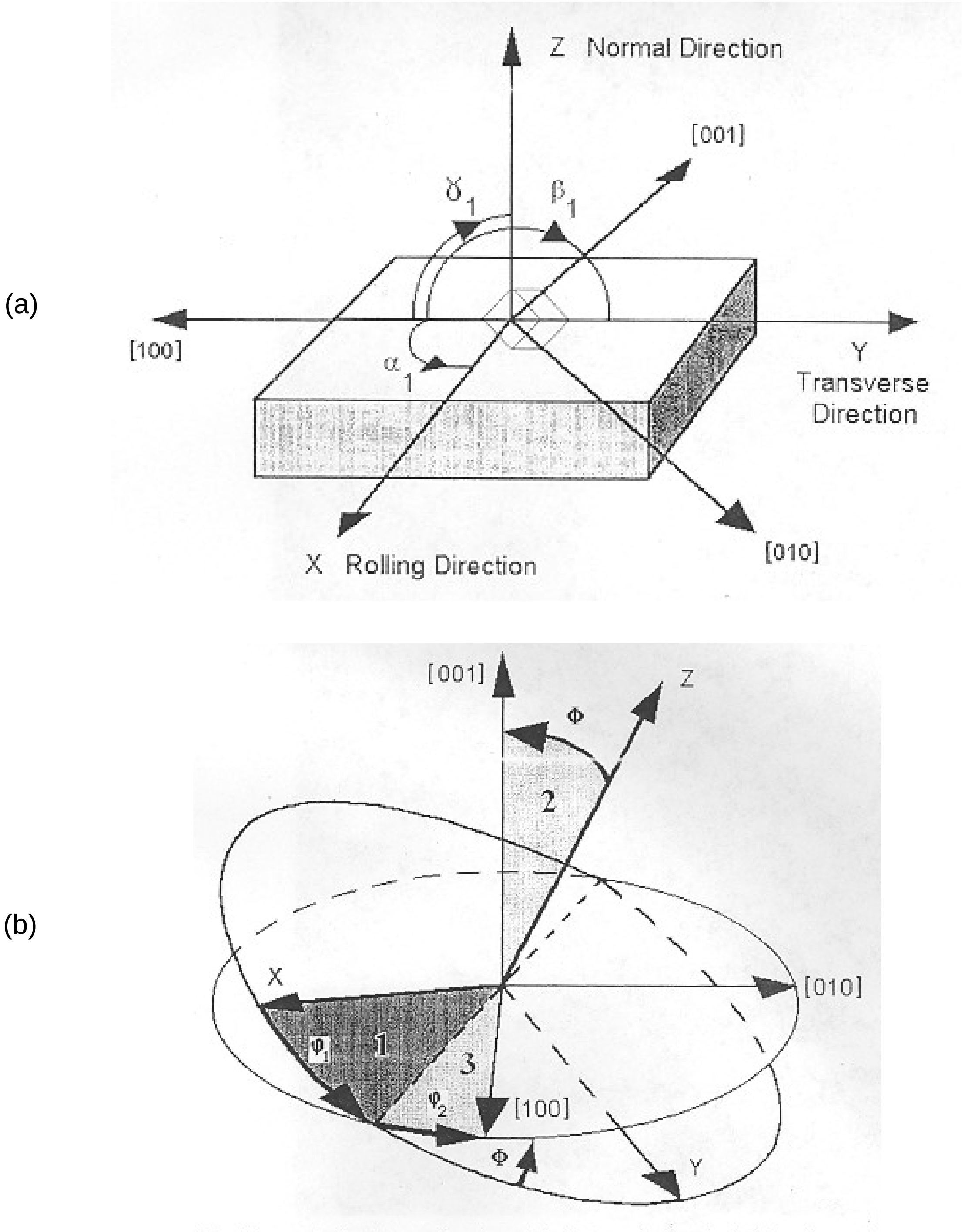
(a)
Z Normal Direction
[001]
γ_1
β_1
[100]
α_1
Y
Transverse Direction
X Rolling Direction
[010]
(b)
[001]
Z
Φ
2
X
[010]
φ_1
1
3
φ_2
[100]
Φ
Y

Figure 2. Orientation relation between the orthogonal sample reference directions and the orthogonal crystal reference directions: (a) Geometry in terms of angles between the two systems of axes (for clarity, only the angles α_1, β_1, and γ_1 are shown) and (b) Euler angles using the Bunge convention [11].

(a) = Figure 2.1 and (b) = Figure 2.7 from Randle and Engler book.

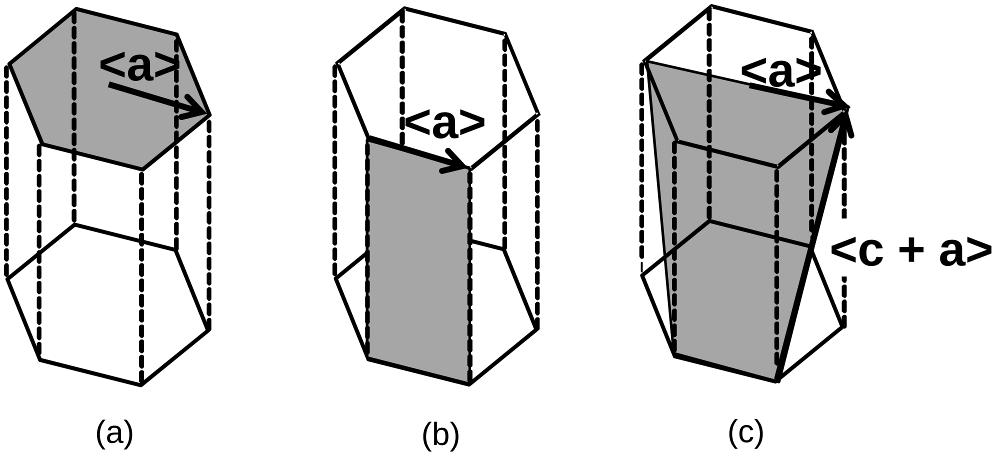

Figure 3. Common slip systems for hcp (alpha) titanium crystals: (a) basal <a>, (b) prism <a>, and (c) pyramidal <c+a>.

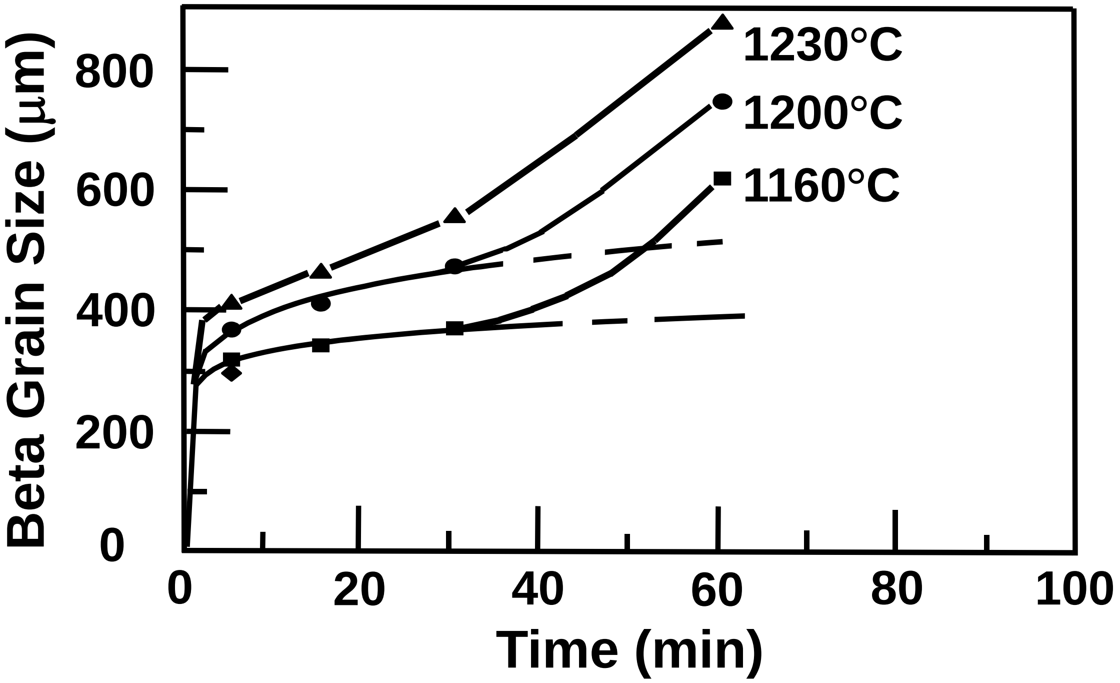

Figure 4. Observations of beta grain-growth in Ti-6Al-4V sheet with a strong initial texture, showing periods of rapid and slow growth [22].

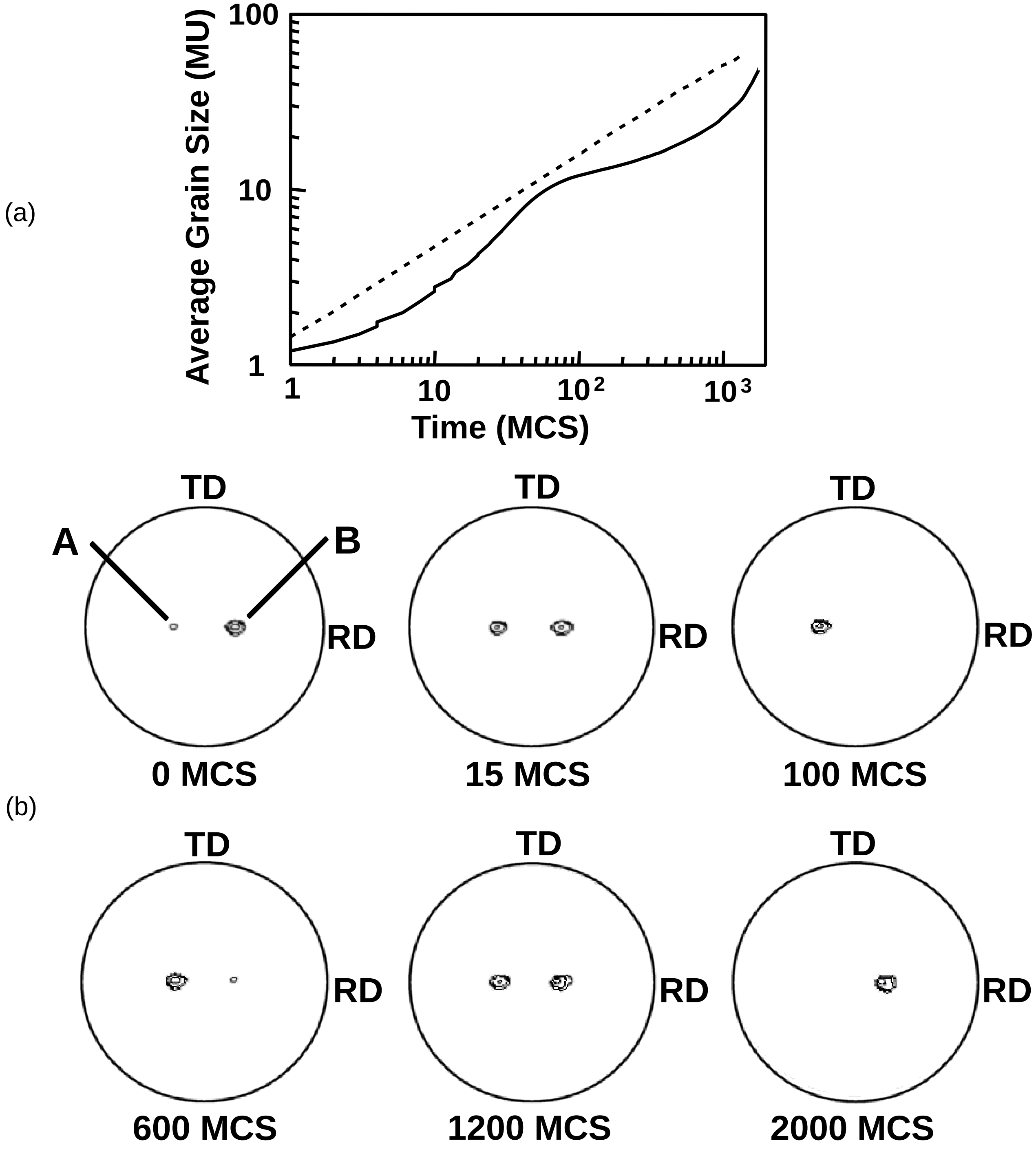

Figure 5. Monte-Carlo model simulation of texture-controlled grain growth for a material with two texture components: (a) Comparison of predicted grain-growth kinetics (solid line) and normal grain-growth kinetics (broken line) and (b) simulated (100) pole figures after various times. MU ~ model lattice units, MCS ~ Monte-Carlo steps. In (b), the iso-intensity lines correspond to 1, 2, 5, 10, and >30 times random, and the 010 and 001 poles are not shown for clarity. [25]

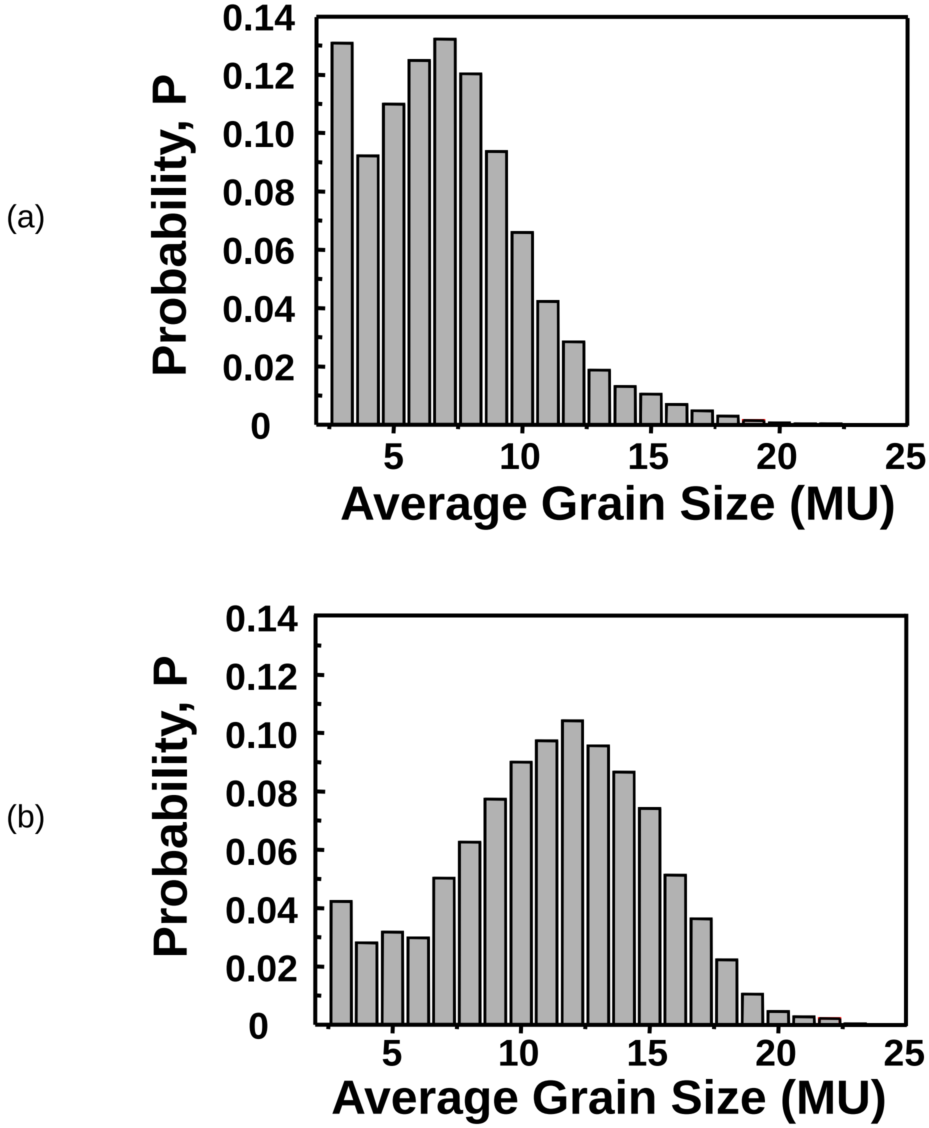

Figure 6. Monte-Carlo model predictions of the grain-size distributions after 15 Monte-Carlo steps for the simulation of texture-controlled grain growth in a material with two texture components: (a) For the entire material and (b) for the grains belonging to texture component A. MU ~ model lattice units. [25]

(a)

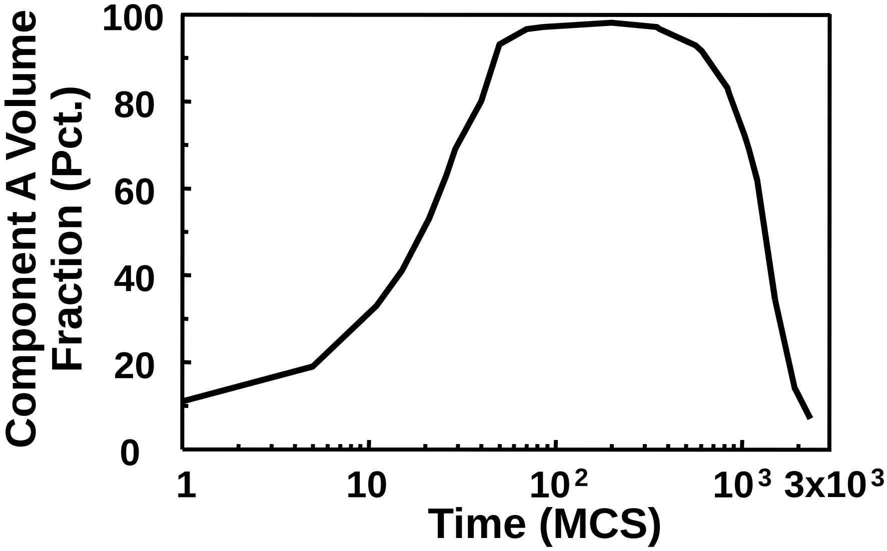

(b)

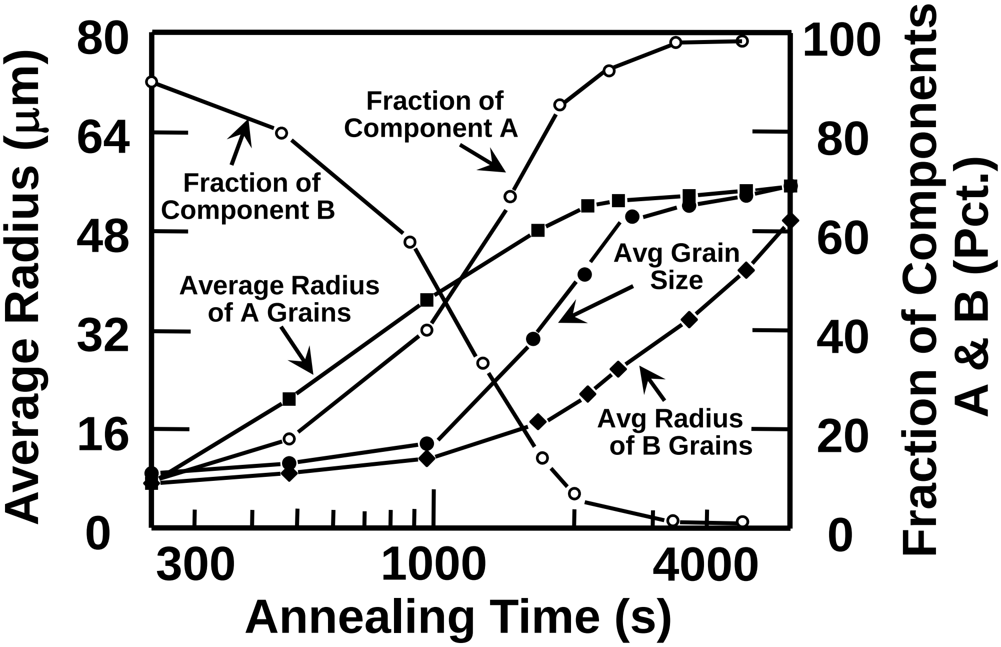

Figure 7. Predictions of the volume fraction of the texture components and the grain size as a function of annealing time for a two-component initial texture using: (a) an MC method [25] and (b) an analytical approach [27]. The labels for components A and B in (b) have been switched from those in Reference 27 in order to coincide with the nomenclature in Reference 25.

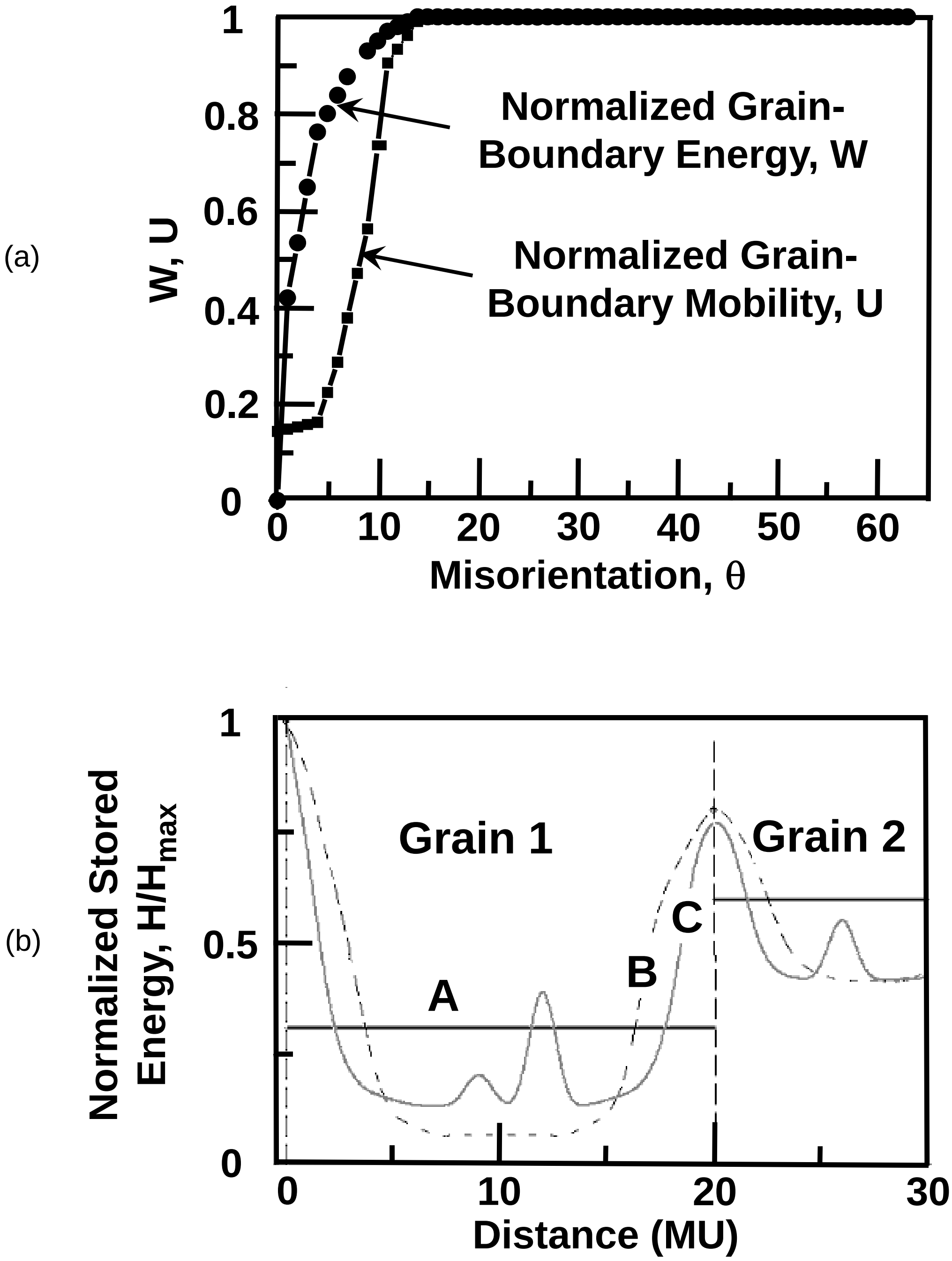

Figure 8. Baseline dependences of (a) grain-boundary energy and mobility (m_a =1) on misorientation and (b) stored-energy on location used in MC simulations of recrystallization and grain growth [34].

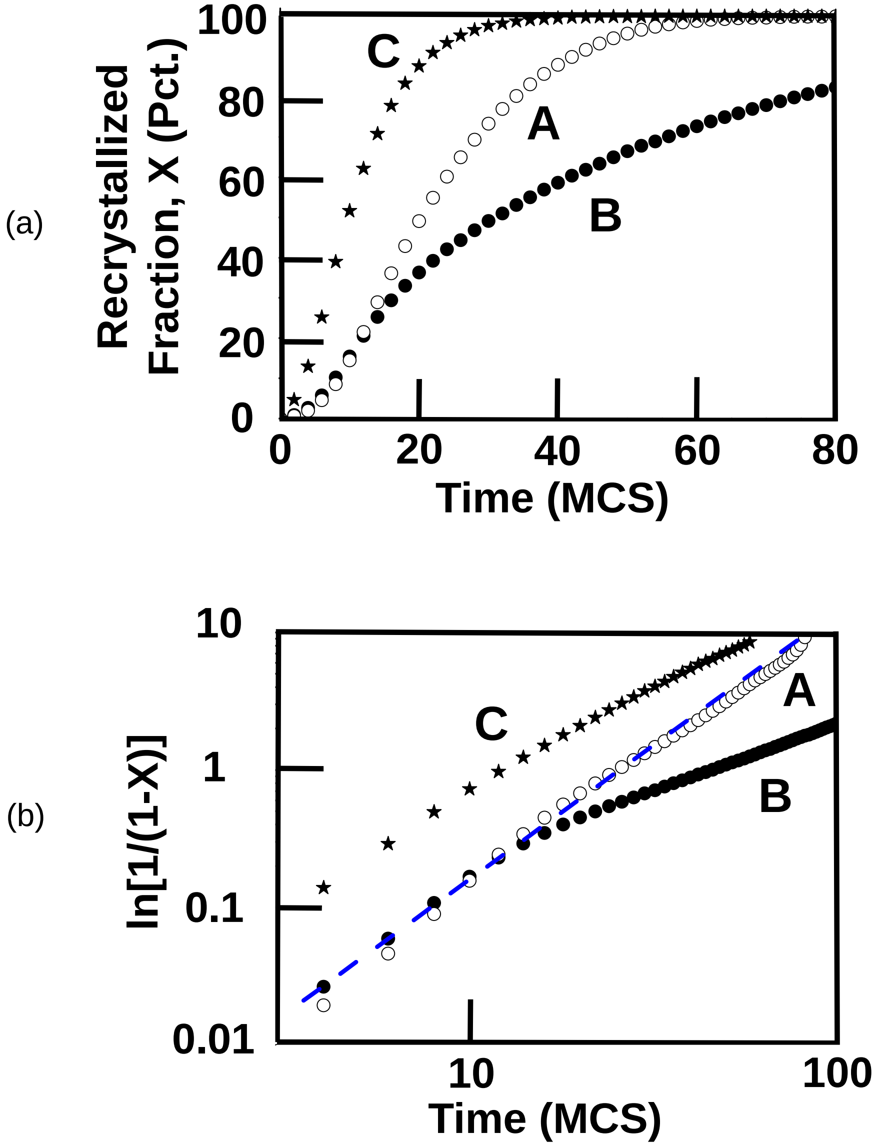

Figure 9. MC simulation predictions of the effect of initial stored-energy distribution on recrystallization, assuming randomly-oriented nuclei: (a) Recrystallized fraction X and (b) corresponding Avrami plots [34]. The letters in the figures refer to the stored-energy distributions shown in Figure 8b.

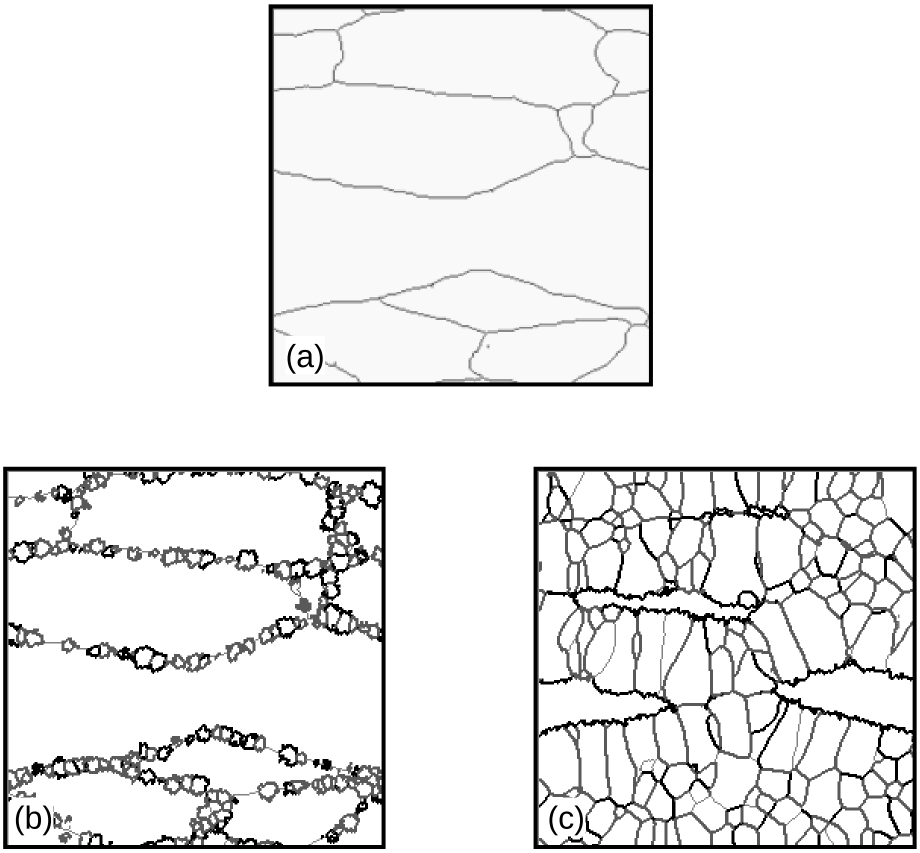

Figure 10. MC-predicted dependence of microstructure evolution in an initially wrought material (shown in (a)) after 100 MCS assuming identical nuclei orientations and a mobility of the special boundaries which was (b) the same or (c) 40 pct. higher than that of other non-special high-angle boundaries [34].

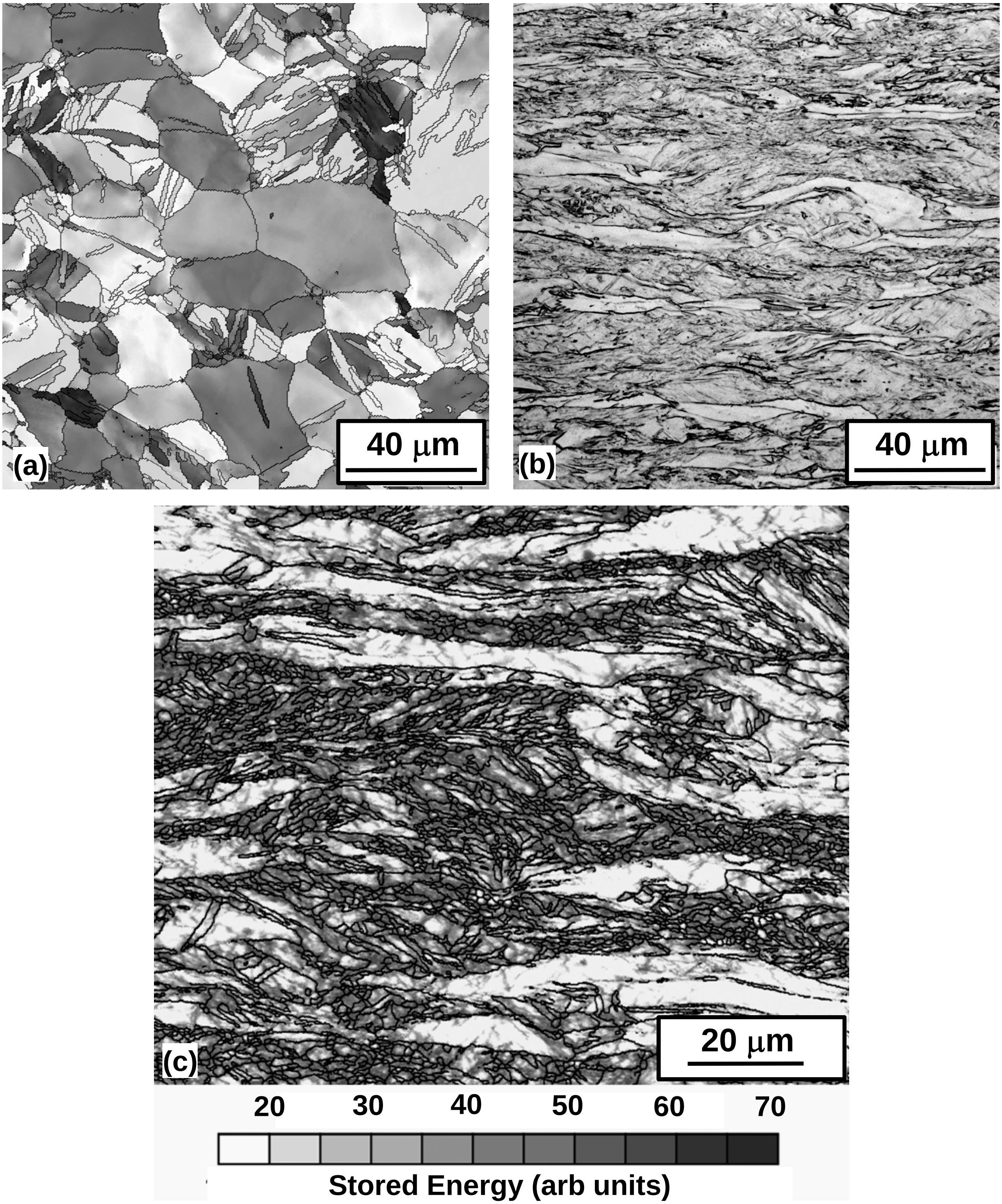
(a)
40 μm
(b)
40 μm
(c)
20 μm
20
30
40
50
60
70
Stored Energy (arb units)

Figure 11. Microstructures developed during cold rolling of CP titanium to a thickness reduction of (a) 20 pct. or (b) 60 pct. Figure (c) shows an EBSD image-quality map for material cold-rolled to a 60-pct. reduction. The rolling direction is horizontal, and the sheet normal direction is vertical in all micrographs. [14, 40, 42]

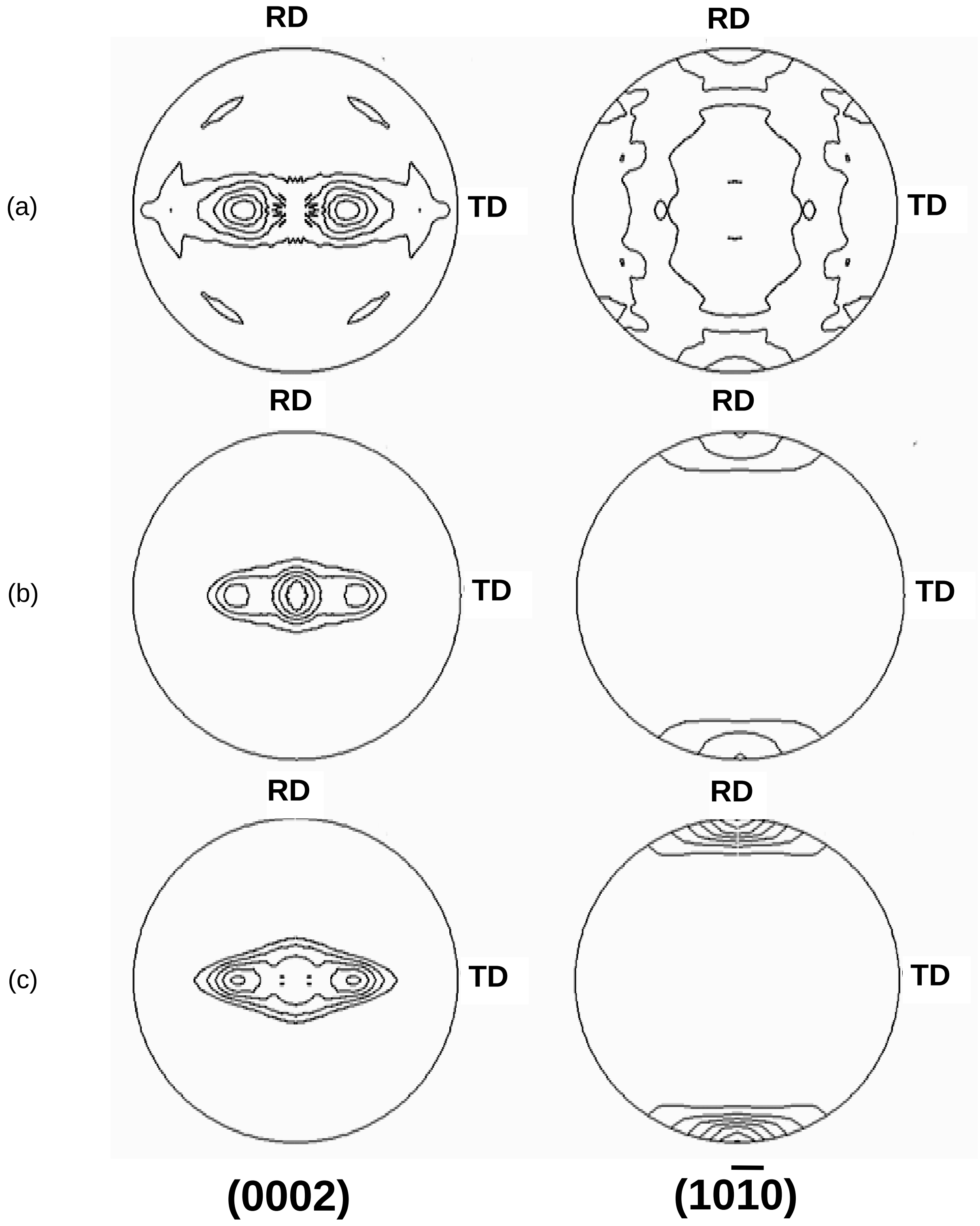

Figure 12. Pole figures for CP titanium cold rolled to percent thickness reductions of (a) 0, (b) 40, and (c) 60 [14]. The maximum x-random texture intensities were (a) 4.4. (b) 3.9, and (c) 3.7. The contour levels for all pole figures are 1.5, 2.0, 2.5,…7.5.

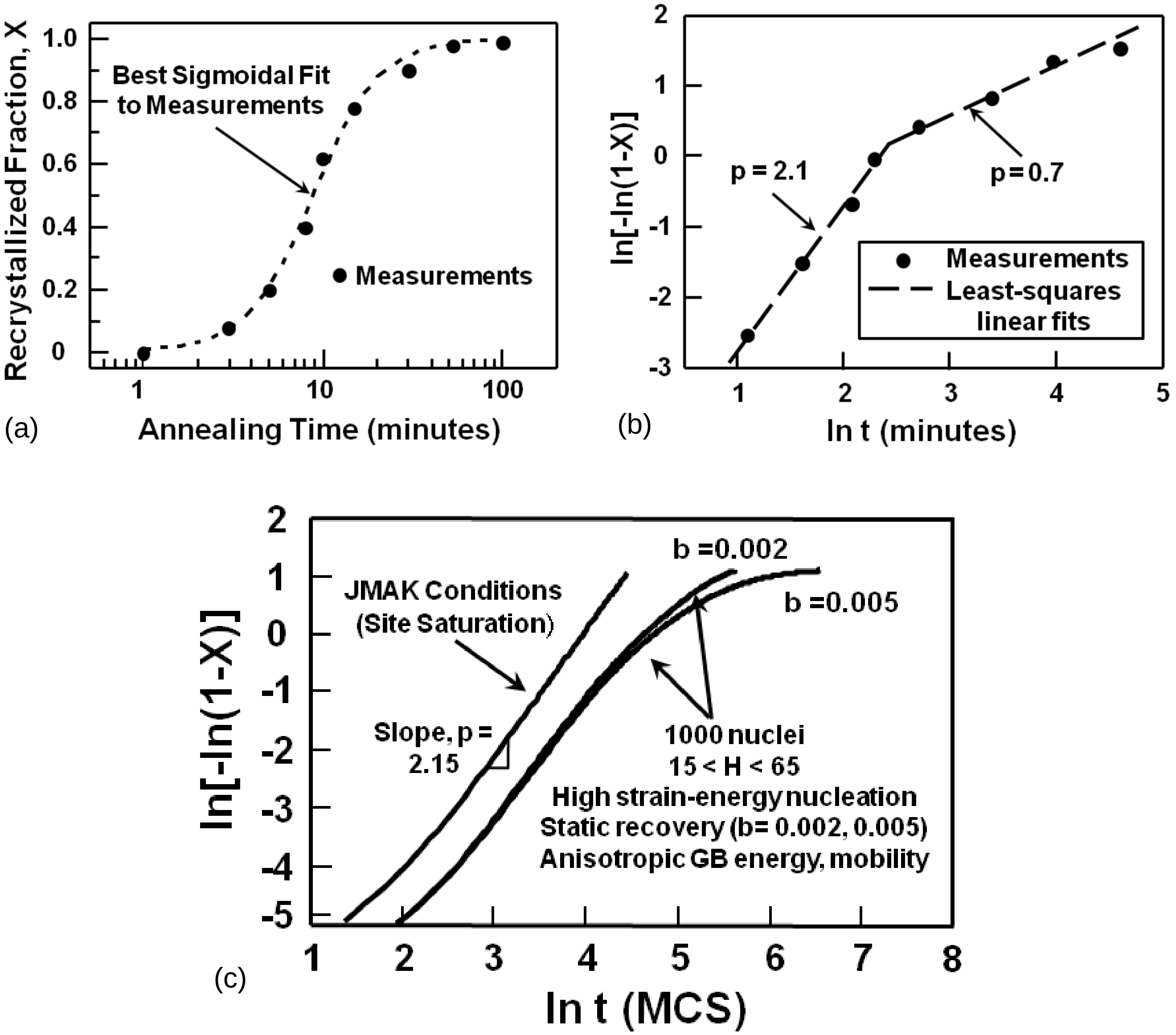

Figure 13. Static recrystallization behavior of CP titanium rolled to a thickness reduction of 60 pct. and annealed at 600°C: (a) Measured recrystallization kinetics, (b) the corresponding experimental Avrami plot, and (c) predicted kinetics from an MC simulation [42].

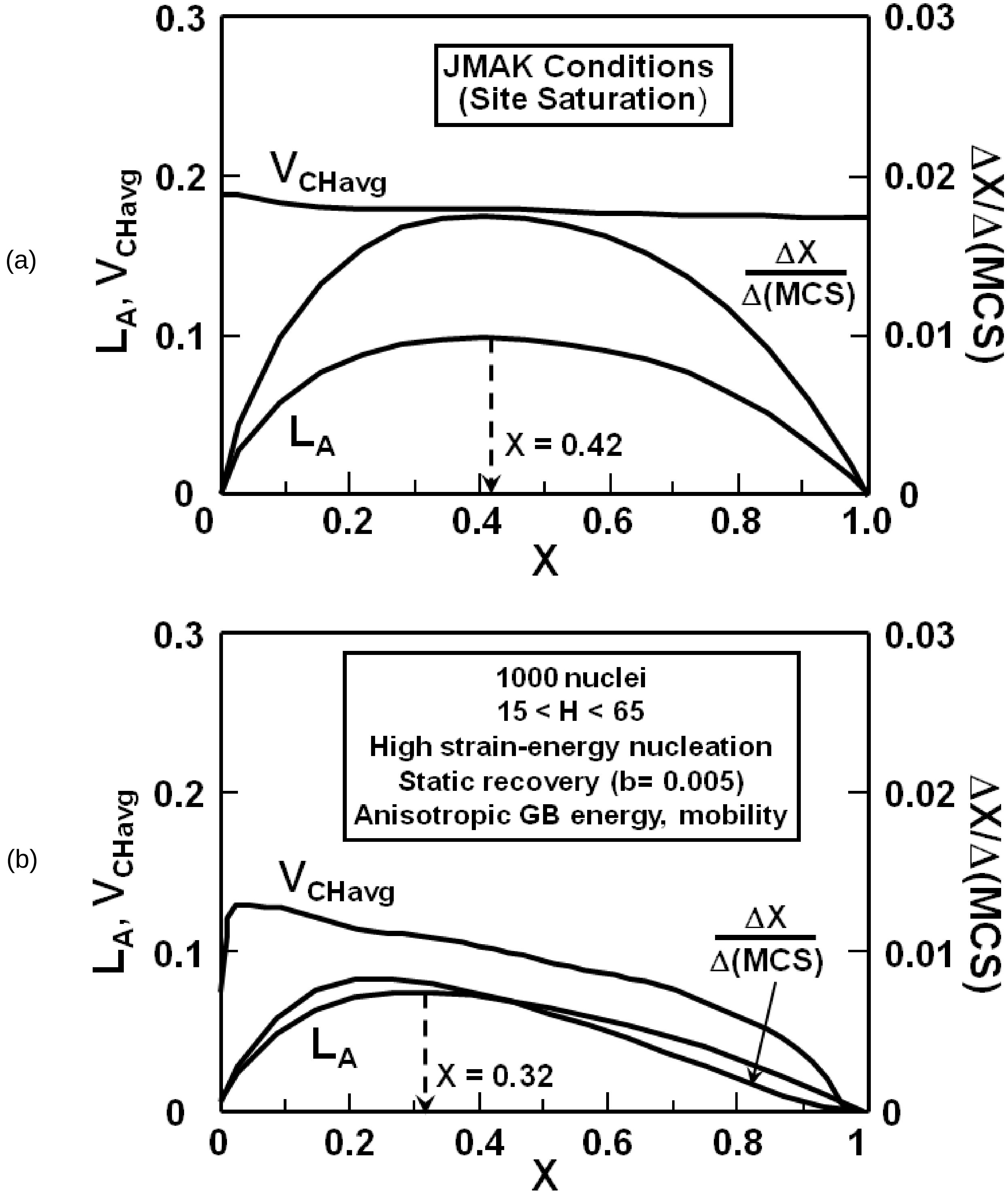

Figure 14. MC predictions of the dependence on recrystallized fraction X of the average velocity (V_{CH}) and total length per unit area (L_A) of the recrystallization front and the rate of recrystallization ($\Delta X/\Delta MCS$) for (1) the classical JMAK condition and (b) a condition involving recovery, heterogeneous nucleation at sites of high stored energy, and anisotropic grain-boundary properties [42].

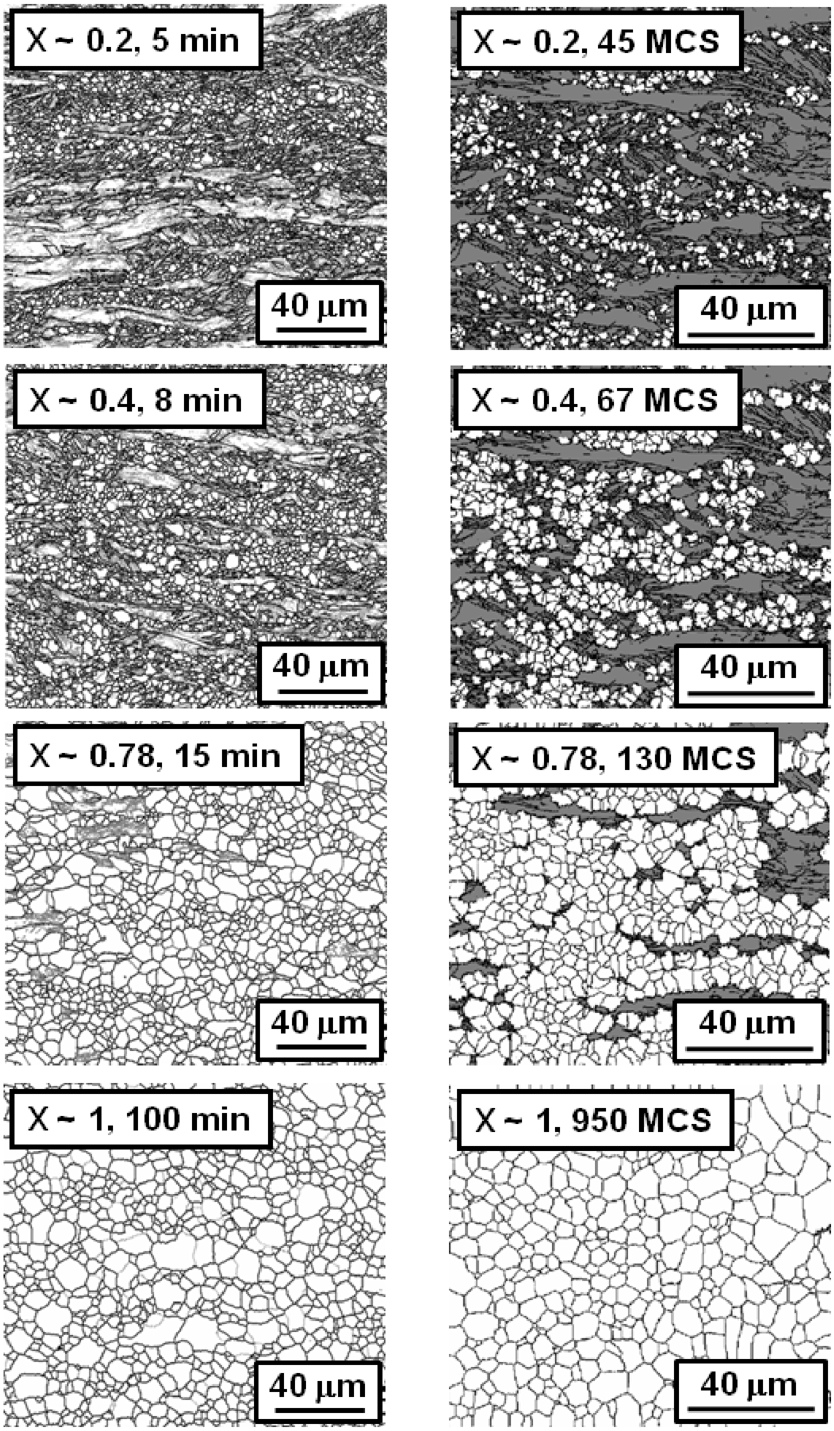
X ~ 0.2, 5 min
40 μm
X ~ 0.2, 45 MCS
40 μm
X ~ 0.4, 8 min
40 μm
X ~ 0.4, 67 MCS
40 μm
X ~ 0.78, 15 min
40 μm
X ~ 0.78, 130 MCS
40 μm
X ~ 1, 100 min
40 μm
X ~ 1, 950 MCS
40 μm

(a) (b)

Figure 15. Comparison of (a) experimental observations and (b) MC predictions of microstructure evolution during recrystallization of CP titanium cold-rolled to a 60-pct. thickness reduction and then annealed at 600°C [42].

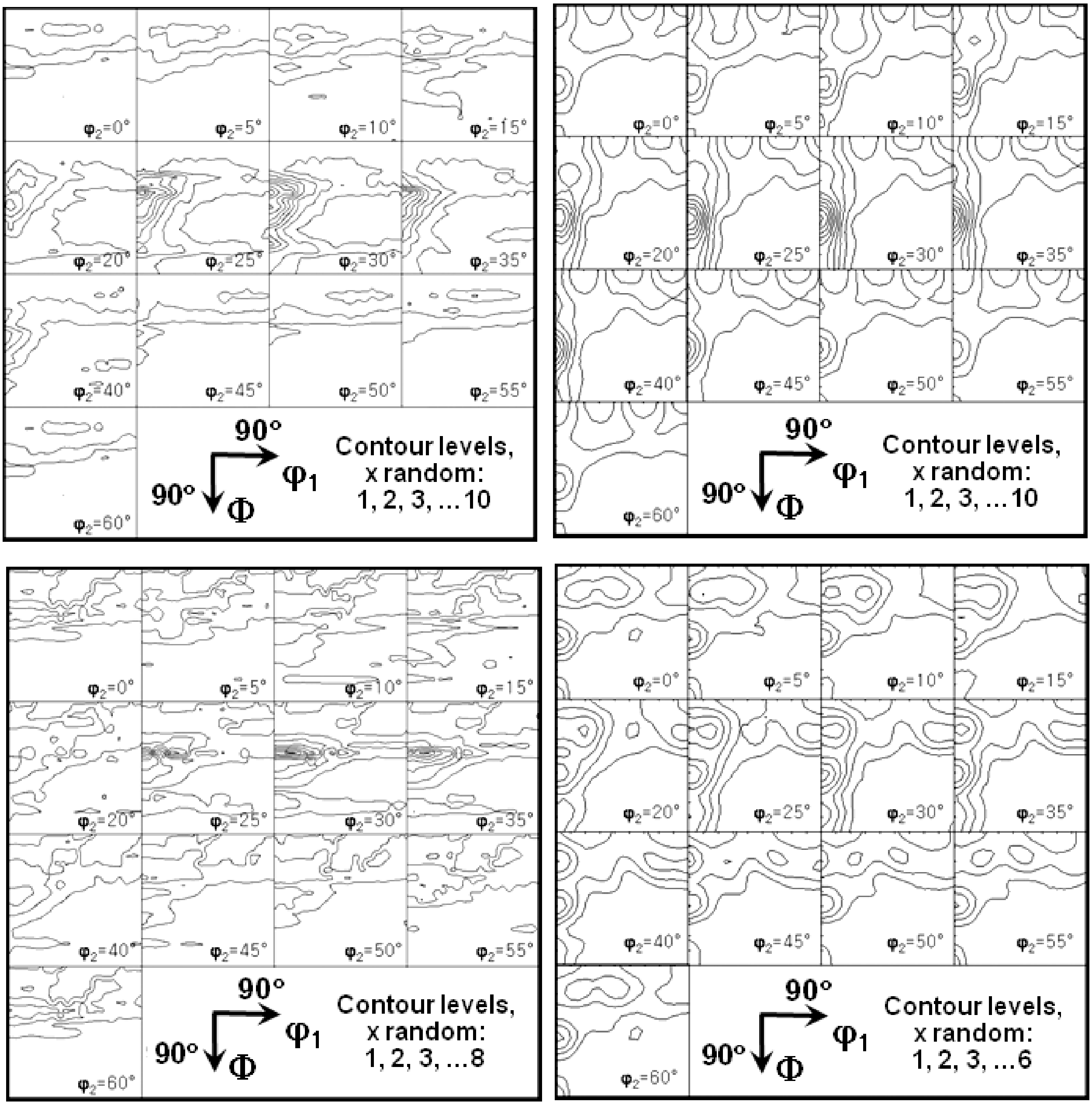

(a) (b)

Figure 16. Comparison of (a) measured and (b) MC-predicted textures developed during recrystallization of CP titanium cold-rolled to a 60-pct. thickness reduction and then annealed at 600°C. In both (a) and (b), the ODF on the top is for the as-deformed condition, and that on the bottom is for the fully recrystallized condition [42].

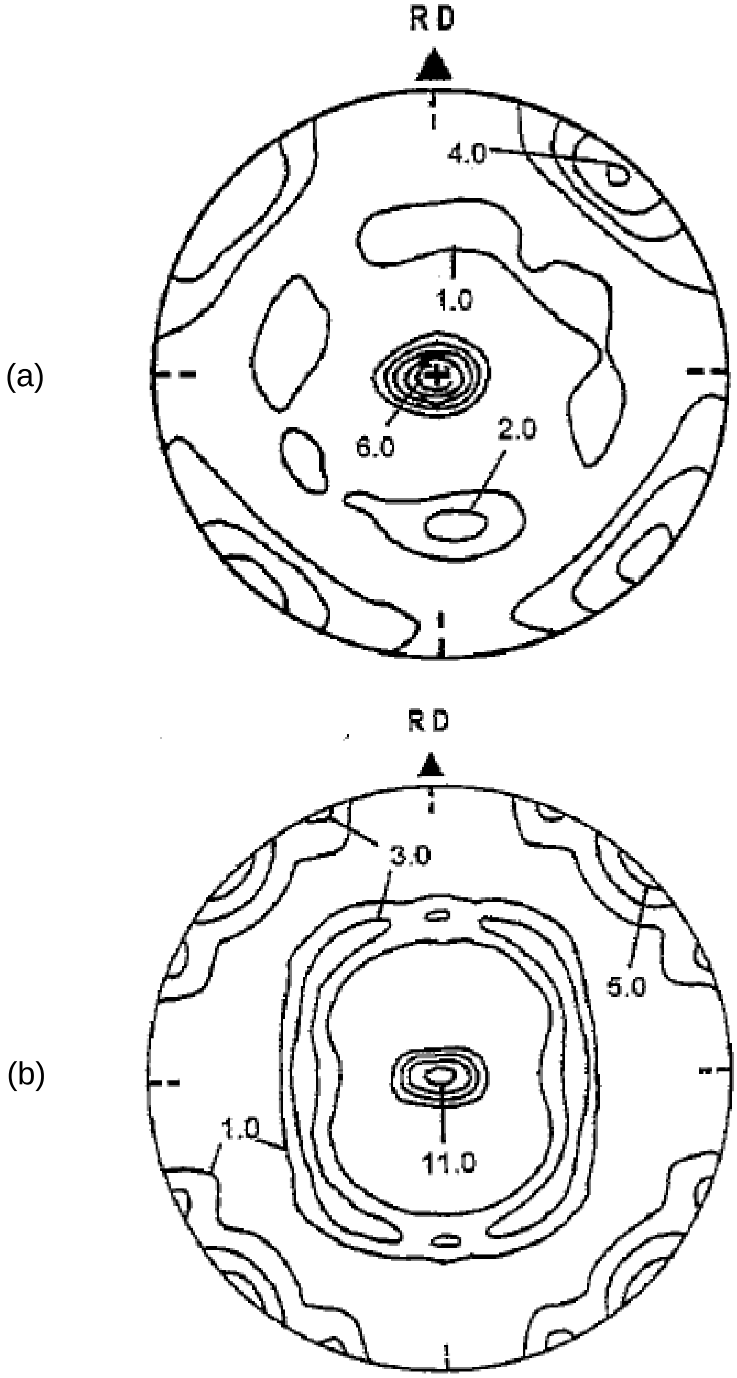

Figure 17. Comparison of (a) measured and (b) predicted (100) beta-phase pole figures for Ti-6Al-4V plate hot rolled to a 75-pct. thickness reduction in the beta phase field [48].

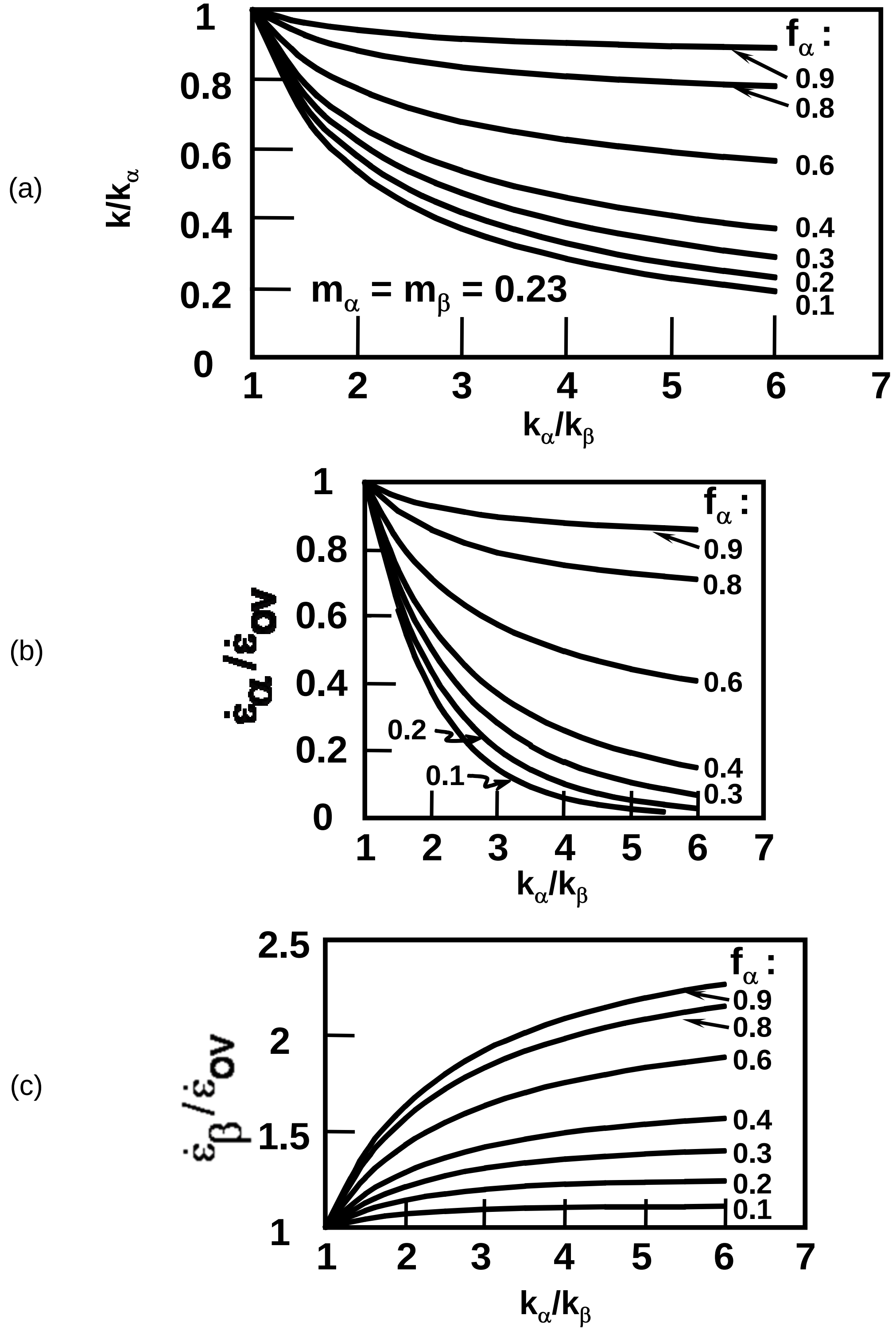

Figure 18. Predictions from an approximate self-consistent model for strain partitioning in a two-phase material with a rate sensitivity of 0.23. The graphs show the dependence on the ratio k_α/k_β and the volume fraction of the harder phase f_α of (a) the aggregate strength coefficient k and (b, c) the strain rates in the harder phase ($\dot{\varepsilon}_\alpha$) and softer phase($\dot{\varepsilon}_\beta$) relative to the overall (aggregate) strain rate($\dot{\varepsilon}_{ov}$) [56].

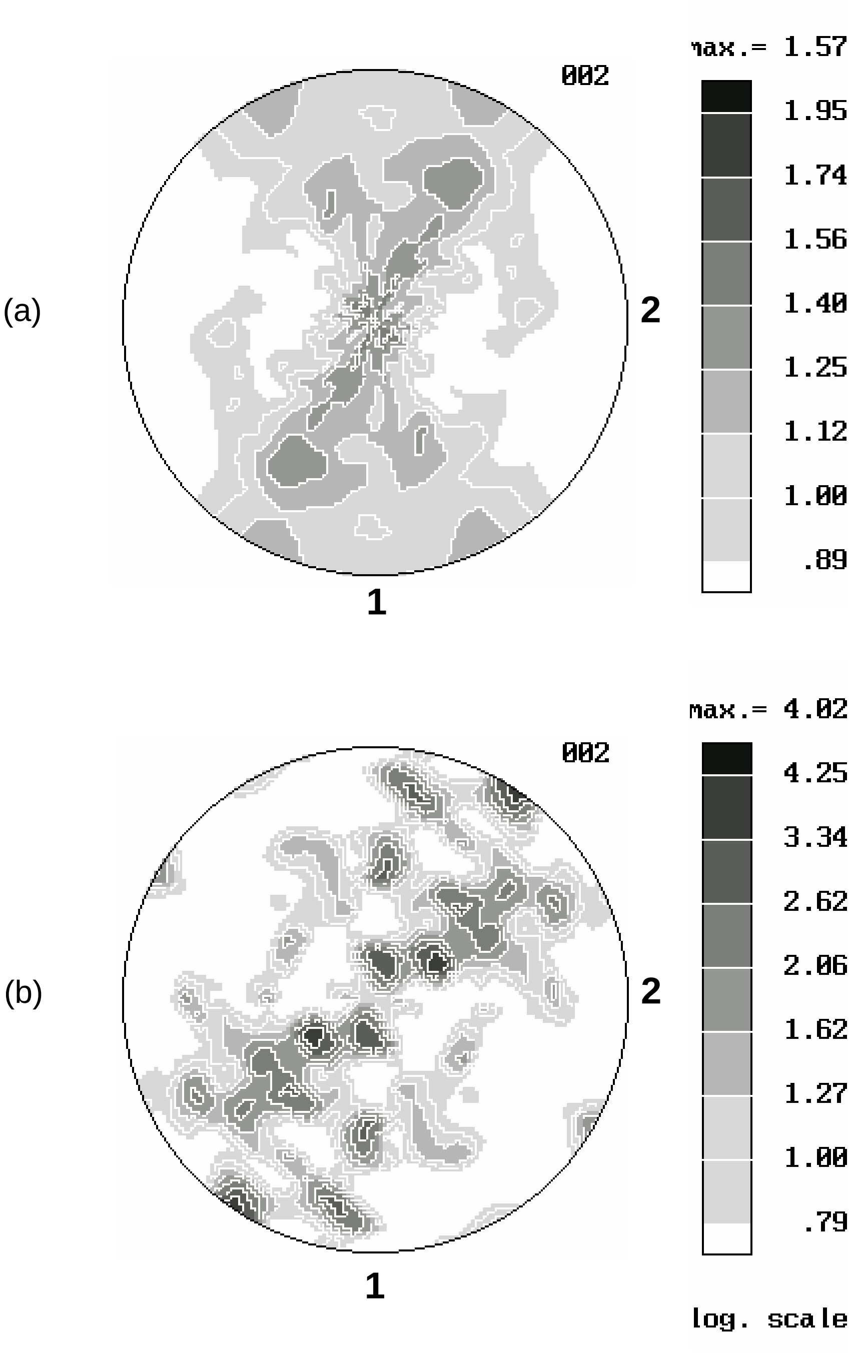

Figure 19. Comparison of the deformation texture (in terms of (0001) pole figures) developed in the primary alpha phase at the corner location of a Ti-6Al-4V billet which was pancake forged at 955°C: (a) measured and (b) predicted [52].

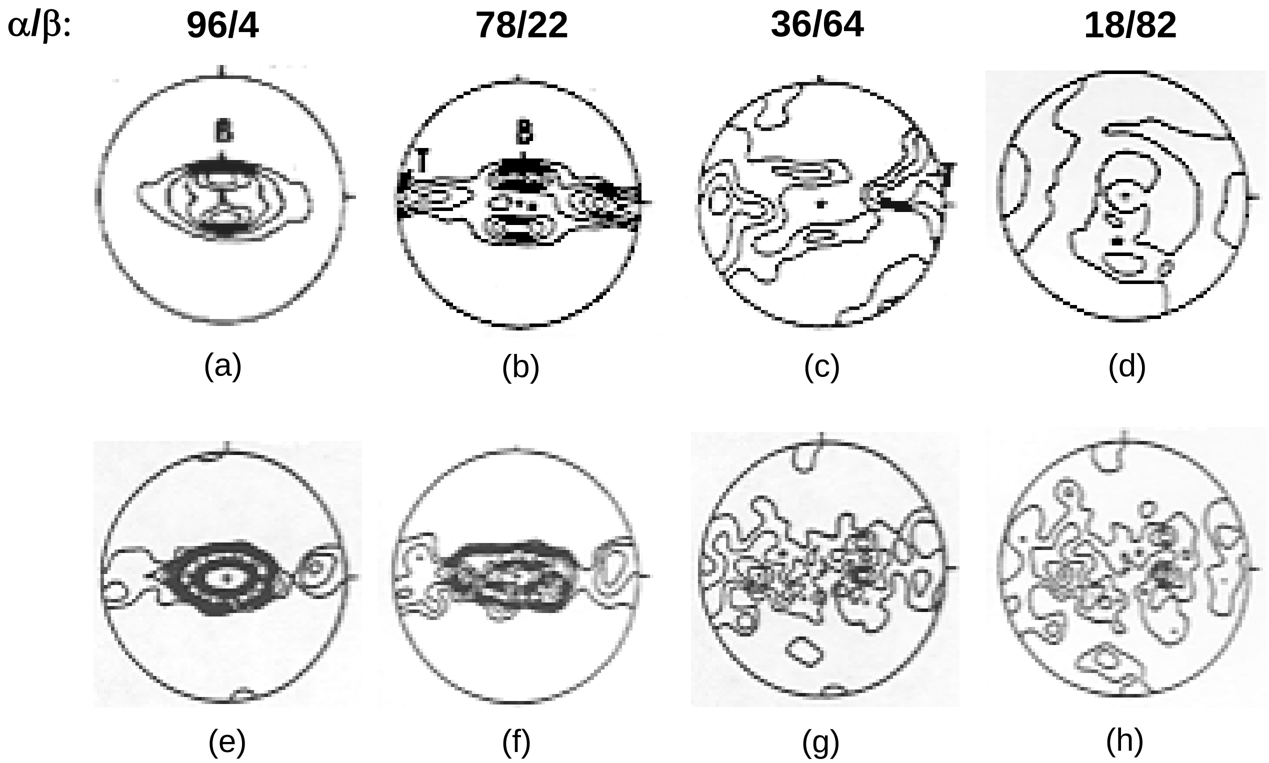

Figure 20. Comparison of (a-d) measured and (e-h) simulated alpha-phase (0001) pole figures for heavily-rolled titanium alloys having alpha/beta volume fractions (in pct.) of (a, e) 96/4, (b, f) 78/22, (c, g) 36/64, and (d, h) 18/82 [59].

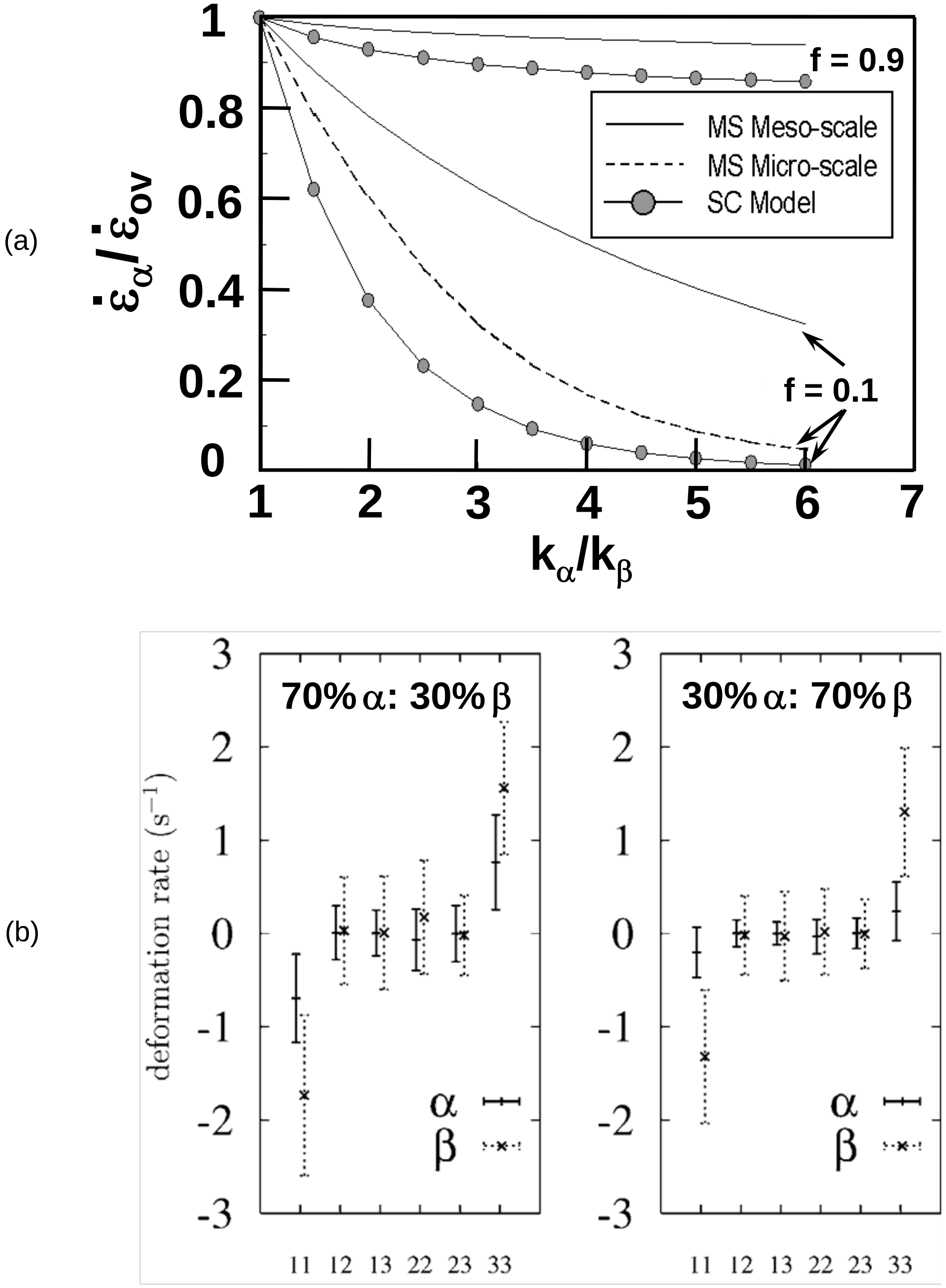

ND= ‘1’, TD = ‘2’, RD = ‘3’

Figure 21. Strain partitioning in two-phase alloys: (a) Comparison of CPFEM meso-scale and micro-scale model predictions with those from a self-consistent model [62] and (b) CPFEM predictions of the strain components in the alpha and beta phases during rolling of titanium plate with two different volume-fraction ratios [63].

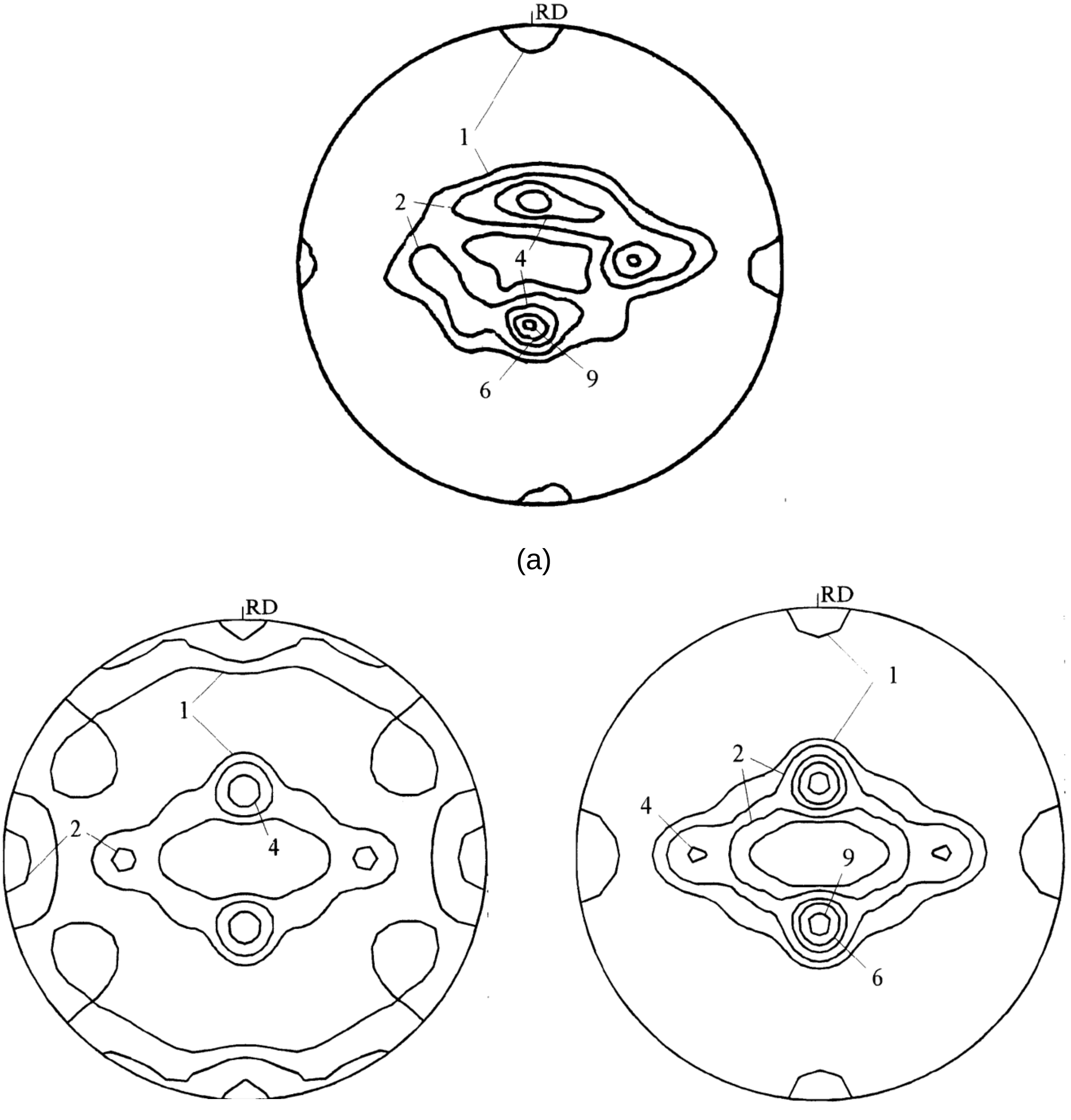

(a)

(b)

(c)

Figure 22. Comparison of (0001) alpha-phase pole figures for Ti-6Al-4V plate that was heat treated high in the alpha + beta phase field and then rapidly cooled: (a) Measured [64], (b) predicted assuming random variant selection [66], and (c) predicted assuming biased variant selection [66].

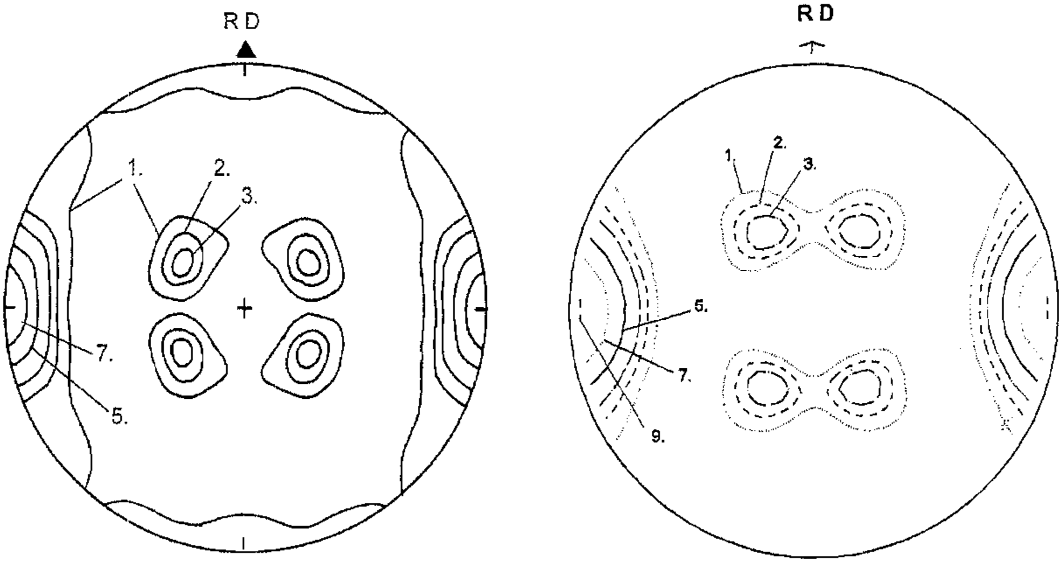

(a)

(b)

Figure 23. Comparison of (0001) pole figures for colony-alpha formed during cooling following hot rolling of Ti-6Al-4V plate to a 75-pct. thickness reduction in the beta-phase field: (a) Measured and (b) predicted using a Taylor-type crystal-plasticity model and alpha-variant selection based on relative slip-system activity [67].